

# Alpine orogenic evolution from subduction to collisional thermal overprint: The $^{40}\text{Ar}/^{39}\text{Ar}$ age constraints from the Valaisan Ocean, central Alps

Michael Wiederkehr,<sup>1,2</sup> Masafumi Sudo,<sup>2</sup> Romain Bousquet,<sup>2</sup> Alfons Berger,<sup>3</sup> and Stefan M. Schmid<sup>1,4</sup>

Received 23 March 2009; revised 15 July 2009; accepted 1 September 2009; published 19 December 2009.

[1] The investigated HP/LT metasedimentary units of the Valaisan and adjacent European domains occupy a key position in the Alpine belt for understanding the transition from early subduction-related HP/LT metamorphism to collision-related Barrovian overprint and the evolution of mountain belts in general. The timing of high-pressure metamorphism, subsequent retrogression and following Barrow-type overprint was studied by  $^{40}\text{Ar}/^{39}\text{Ar}$  dating of biotite and several white mica generations that are well characterized in terms of mineral chemistry, texture and associated mineral assemblages. Four distinct age populations of white mica record peak pressure conditions (42–40 Ma) and several stages of subsequent retrograde metamorphic evolution (36–25 Ma). Biotite isotopic analyses yield consistent apparent ages that cluster around 18–16 Ma for the Barrow-type thermal overprint. The recorded isotopic data reveal a significant time gap in the order of some 20 Ma between subduction-related HP/LT metamorphism and collision-related Barrovian overprint, supporting the notion of a polymetamorphic evolution associated with a bimodal P-T path. **Citation:** Wiederkehr, M., M. Sudo, R. Bousquet, A. Berger, and S. M. Schmid (2009), Alpine orogenic evolution from subduction to collisional thermal overprint: The  $^{40}\text{Ar}/^{39}\text{Ar}$  age constraints from the Valaisan Ocean, central Alps, *Tectonics*, 28, TC6009, doi:10.1029/2009TC002496.

## 1. Introduction

[2] Understanding the metamorphic evolution of the earth's crust requires well-constrained time data. Such data are of particular importance regarding the geodynamics of subduction, followed by unroofing in a collisional scenario later on. Numerical models explore the effects of the thermal structure acquired during subduction on subsequent stages of

the metamorphic history during collision and exhumation [e.g., Bousquet *et al.*, 1997; Jamieson *et al.*, 1998; Roselle *et al.*, 2002; Goffé *et al.*, 2003]. In order to test such models by field studies we do not only need the constraints on the metamorphic evolution in P-T space that are widely available by now [e.g., Oberhänsli *et al.*, 2004] but also more data on the evolution in time [e.g., Berger and Bousquet, 2008]. The central Alps provide a unique example of an area, from which an unusually large and unique data set on the metamorphic evolution is available [e.g., Bousquet *et al.*, 2008], but where the timing of the early blueschist facies stage of metamorphism is still very poorly constrained.

[3] The Alps formed as a result of subduction- and subsequent collision-related processes due to plate convergence between Europe and Adria in Mesozoic and Cenozoic times. The distal European continental margin and Tethyan oceanic lithosphere, including an intervening microcontinent (Briançonnais), were subducted and partially incorporated into an accretionary orogenic wedge sandwiched between the overlying Adria-derived nappes (Austroalpine) and the southward subducting underlying European plate [e.g., Trümpy, 1960; Frisch, 1979; Tricart, 1984; Le Pichon *et al.*, 1988; Schmid *et al.*, 1996]. Early stage subduction-related processes took up most of the plate convergence and led to the formation of high-pressure belts that strike parallel to the orogen [e.g., Oberhänsli *et al.*, 2004]. It is now widely accepted that the Alpine orogenic belt incorporated three high-pressure belts, one being of Cretaceous age and only affecting the continental Austroalpine domain [e.g., Thöni, 2006] while two Cenozoic belts are related to subduction processes within two branches of the Alpine Tethys, i.e., the southern Piedmont-Liguria and the northern Valaisan Ocean, respectively, separated by the Briançonnais microcontinent [e.g., Frisch, 1979; Stampfli, 1993; Oberhänsli, 1994; Stampfli *et al.*, 1998; Froitzheim *et al.*, 2003].

[4] Relics of the Piedmont-Liguria Ocean exposing in the Zermatt-Saas ophiolite are characterized by a spectacular and well-known HP/LT metamorphic event [e.g., Bearth, 1967; Chinner and Dixon, 1973; Ernst and Dal Piaz, 1978], for which numerous isotopic data are available by now, albeit their geodynamical interpretation is still difficult (see review by Berger and Bousquet [2008]). This abundance of isotopic data contrasts with the scarcity of data from the northern and more external, at least partly oceanic, Valaisan units. Within Switzerland and the adjacent Italian-French Alps, the Valaisan mainly exposes voluminous low-grade Fe-Mg carpholite-bearing HP/LT metasediments [Goffé and Oberhänsli, 1992;

<sup>1</sup>Geologisch-Paläontologisches Institut, Universität Basel, Basel, Switzerland.

<sup>2</sup>Institut für Geowissenschaften, Universität Potsdam, Potsdam, Germany.

<sup>3</sup>Institut for Geografi og Geologi, Københavns Universitet, Copenhagen, Denmark.

<sup>4</sup>Now at Institut für Geologische Wissenschaften, Freie Universität Berlin, Berlin, Germany.

*Oberhänsli, 1994; Goffé and Bousquet, 1997; Bousquet et al., 1998, 2002*], associated with scarce and isolated fragments of mafic and ultramafic bodies. The timing of HP/LT metamorphism in this northern high-pressure belt is not only very poorly constrained but the few available ages grossly scatter [*Berger and Bousquet, 2008*]. The only isotopic data available for metasediments around the Petit St. Bernard area yield 34–27 Ma [*Freeman et al., 1998; Cannic et al., 1999*] but have to be considered with great caution due to the fact that the available studies were not aware of the presence of a HP/LT metamorphic event in the Valaisan domain. Hence, there is no reliable geochronological data on the high-pressure overprint of the Valaisan metasediments, and the age of this overprint can only be bracketed to between the HP events in the Briançonnais- and in Europe-derived units (i.e., between 47–42 Ma and 38–35 Ma; see review given by *Berger and Bousquet [2008, and references therein]*). Results reported for high-pressure metamorphism in the Antrona and Balma eclogites yielded ages between 46 and 39 Ma [*Liati et al., 2005; Liati and Froitzeim, 2006; Herwartz et al., 2008*], but the attribution of these units to the Valaisan is controversial. Radiometric ages that claim to date the high pressure event in the Eclogite Zone of the Tauern window, a unit that many authors [e.g., *Schmid et al., 2004*] associate with the subduction of the Valaisan Ocean, are extremely controversial and vary between 31.5 Ma [e.g., *Glodny et al., 2005*] and  $\leq 45$  Ma [e.g., *Ratschbacher et al., 2004*].

[5] The area investigated by this study occupies a key location in the central Alps, located at the northeastern edge of the Lepontine dome (Figure 1a). The area offers uninterrupted excellent exposure of metasedimentary units derived from the Valaisan and adjacent distal European domains within which subduction-related HP/LT metamorphism dominates in the northeast (Engadine window and Grisons area) while collision-related Barrow-type amphibolite facies metamorphism dominates in the southwest (Figure 1) [see also *Wiederkehr et al., 2008*]. This allows for collecting samples from a continuous along-strike section and for investigating the geodynamical relationships between these two contrasting tectonometamorphic events. For the first time this study provides geochronological data regarding both stages of a polymetamorphic evolution and from within the same working area located in the central Alps: HP/LT metamorphism including subsequent retrogression, followed by a Barrow-type thermal metamorphic event. We analyzed samples that are well described in terms of their metamorphism [see *Wiederkehr et al., 2008; Wiederkehr, 2009; Bousquet et al., 1998*] in order to date mineral growth and/or reactions by using  $^{40}\text{Ar}/^{39}\text{Ar}$  techniques. We will present results of in situ  $^{40}\text{Ar}/^{39}\text{Ar}$  dating of successive white mica generations reflecting the subduction-related metamorphism on the one hand, and dating of biotite grown during collision-related Barrovian overprint on the other hand. Additionally  $^{40}\text{Ar}/^{39}\text{Ar}$  stepwise heating experiments on biotite grain separates were performed for comparison with in situ dating and complete the data set. These new data offer the opportunity to test and further quantify the geodynamic evolution proposed by *Wiederkehr et al. [2008]*. Moreover, this work represents a case study that addresses the transition from subduction to

collision in general and thereby provides important field and geochronological data for testing numerical models for the geodynamic evolution of orogenic belts [e.g., *Bousquet et al., 1997; Jamieson et al., 1998; Roselle et al., 2002; Goffé et al., 2003*].

## 2. Tectonometamorphic Background and Sampling Strategy

### 2.1. Geological Setting

[6] The studied area is located at the northeastern edge of the Lepontine dome (Figure 1a) that represents a dome both in a structural and thermal sense. Structurally, this dome consists of Europe-derived basement nappes (Figure 1b; Sub-Penninic after *Schmid et al. [2004]*) that represent the deepest exposures within the central Alps [e.g., *Froitzeim et al., 1996*]. These pre-Mesozoic basement nappes are tectonically overlain by Mesozoic age metasedimentary units derived from both the distal European margin (Sub-Penninic cover nappes and slices) and the Valaisan oceanic domain (Lower Penninic), separated from each other by the Penninic Basal Thrust (Figure 1b). In the easterly adjacent areas the Mesozoic metasediments of the Valaisan domain form up to 15 km thick pile of metasedimentary cover nappes [*Hitz and Pfißner, 1997*] (see crustal-scale transect of *Schmid et al. [1996, Plate 1]*). Due to the general axial plunge of the whole nappe stack to the east, these Valaisan-derived metasediments are seen to be tectonically overlain by nappes derived from the Briançonnais, Piemont-Liguria Ocean, and Austroalpine domain, respectively, still further to the east (Figure 1a). Within the Engadine window (Figures 1a and 1c) the Valaisan Bündnerschiefer are again exposed within a local antiformal dome below the Austroalpine lid.

[7] Lithologically the Valaisan-derived metasediments are a rather monotonous sequence that predominantly consists of calcschists with intercalations of limestones, shales, marls and sandy limestones, deposited in Cretaceous to Eocene times [*Nänny, 1948; Ziegler, 1956; Steinmann, 1994; Steinmann and Stille, 1999*]. In the west the Valaisan Bündnerschiefer are subdivided into Grava and Tomül nappes, based on stratigraphic criteria [*Steinmann, 1994*] (Figure 1b). The metasediments in the Engadine window are built up by the high-pressure Mundin unit, overlain by the low-pressure Arina unit (Figure 1c) [*Bousquet et al., 1998*]. Scarce occurrences of mafic and ultramafic rocks are associated with these metasediments, mainly around Piz Aul and Piz Tomül in the west (Figure 1b) [*Nabholz, 1945*] and around Piz Mundin of the Engadine window in the east (Figure 1c). However, rather large bodies of serpentized peridotite are found below the Grava unit (Aul unit) [*Nabholz, 1945*] and in the Engadine window. The latter are associated with ophicarbonates, serpentinite breccia, metagabbro and metabasalt, forming the so-called Ramosch zone (Figure 1c), interpreted as representing the transition between the continental Briançonnais and the oceanic Valaisan domain [*Florineth and Froitzeim, 1994; Froitzeim et al., 1996*]. These occurrences clearly indicate that at least parts of the Valaisan-derived metasediments were deposited on oceanic crust [*Steinmann, 1994; Steinmann and Stille, 1999*]. In the Valaisan

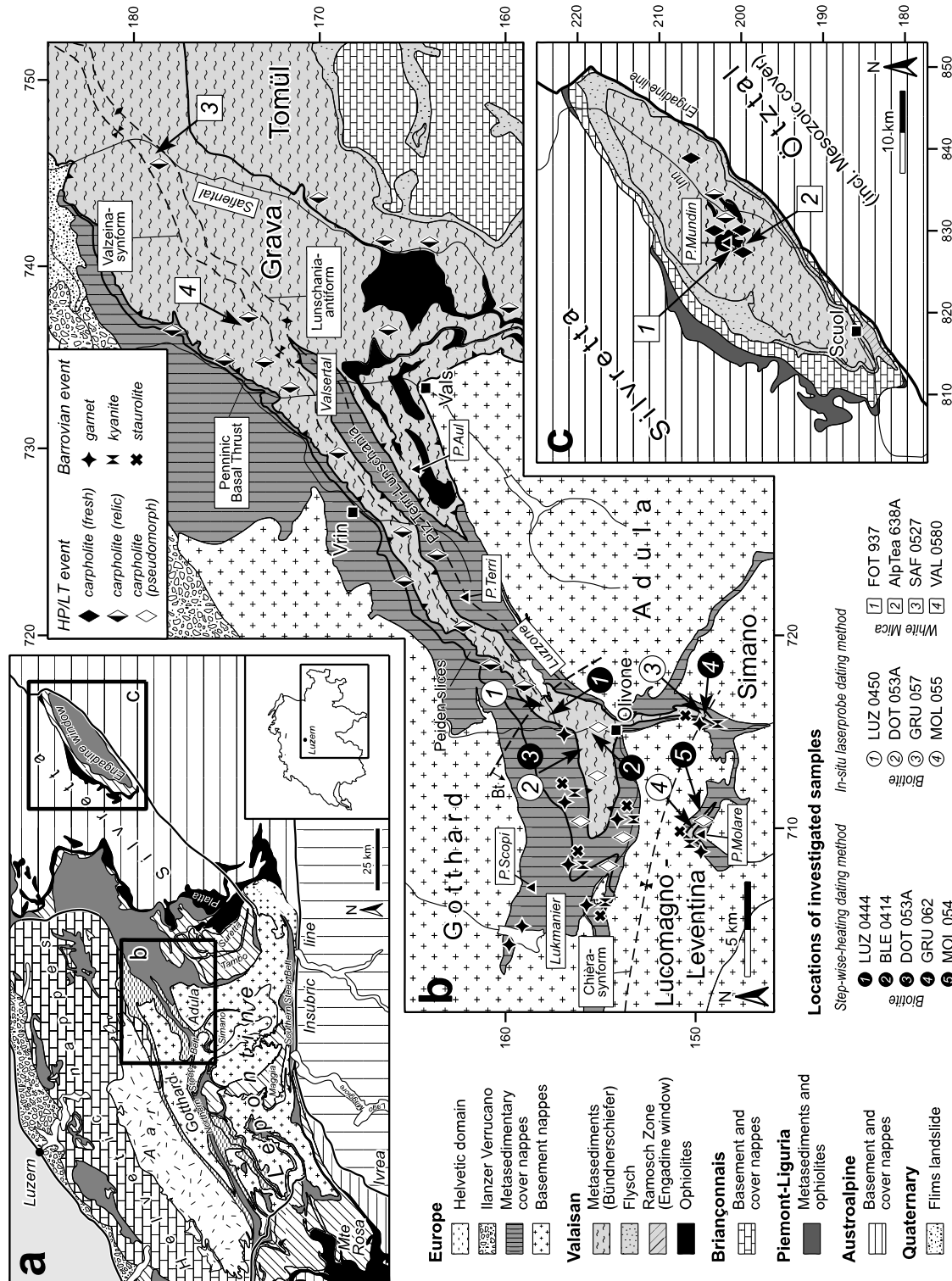


**Figure 1.** Geological map of the investigated area and locations of the studied samples. (a) Tectonic map of the central Alps after Schmid *et al.* [2004]; the two black rectangles indicate the outlines of the more detailed map views shown in Figures 1b and 1c. (b) Detailed map of the Lepontine dome and easterly adjacent areas also indicating the main geographical names mentioned in the text; biotite-in isograds and distribution of indicative minerals are based on the work by Wiederkehr *et al.* [2008, and references therein]. (c) Detailed map of the Engadine window; the distribution of HP/LT minerals is after Bousquet *et al.* [1998].

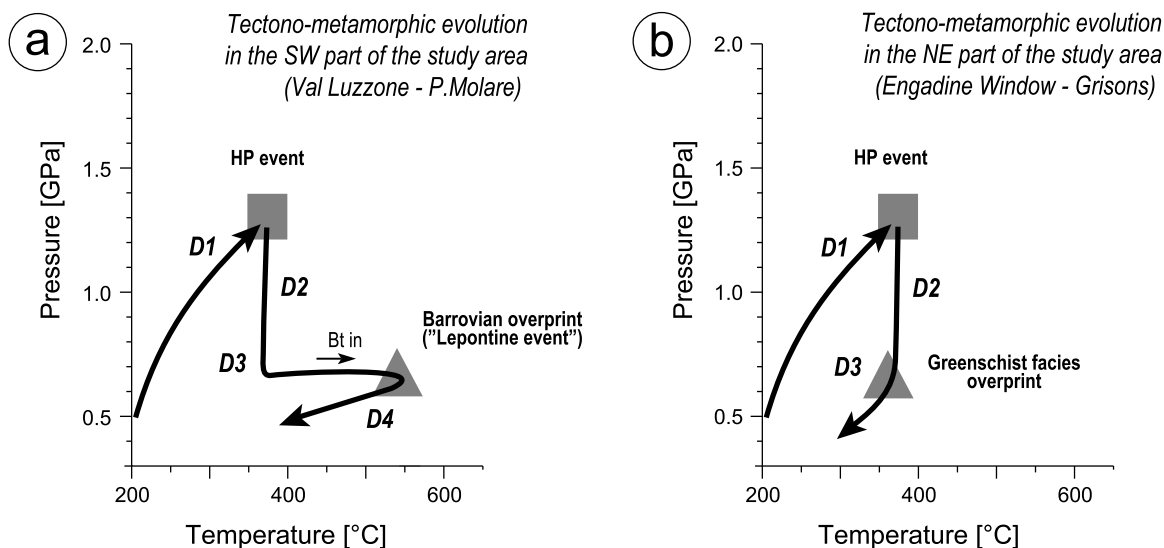


**Figure 2.** Summary of tectonometamorphic evolution (see text for more information). (a) Bimodal P-T path typical for the southwestern part of the study area (NE Lepontine dome) and associated deformation phases, established for the Valaisan- and Europe-derived metasediments. Note that biotite growth is related to Barrovian Lepontine metamorphism that represents a late stage separate heating pulse and follows isothermal or slightly cooling decompression after the early HP/LT event. (b) Single P-T path typical for the northeastern part of the study area, i.e., Valsertal, Safiental, and Engadine window, respectively, characterized by an early HP/LT stage that was only followed by more or less isothermal decompression.

domain there is also clear evidence for subduction-related HP/LT metamorphism under blueschist facies conditions provided by the widespread occurrences of Fe-Mg carpholite in metasediments [Goffé and Oberhänsli, 1992; Oberhänsli et al., 1995; Bousquet et al., 1998] as well as by rare findings of glaucophane in mafic rocks [Oberhänsli, 1978; Bousquet et al., 1998]. Metamorphic conditions of 1.2–1.4 GPa and 350–400°C have been estimated [Bousquet et al., 2002]. It has recently been shown that not only the Valaisan Bündnerschiefer but also parts of the metasedimentary units belonging to the European realm were affected by the same early HP/LT event, as documented by occurrences of Fe-Mg carpholite in both Peiden slices and Piz Terri-Lunschania unit [Wiederkehr et al., 2008; Wiederkehr, 2009].

[8] Only toward the SW were the metasediments of both the European and Valaisan realm affected by a Barrow-type thermal overprint; the temperatures progressively increase southwestwards, i.e., toward the center of the Lepontine thermal dome. Such progressive Barrovian metamorphism is best documented within Europe-derived metasediments (Sub-Penninic cover nappes and slices) due the great chemical variability of these Triassic to lower/middle Jurassic sequences, consisting of metaevaporites, metapelites, calcareous shales, carbonaceous calcschists and shales [Baumer et al., 1961; Probst, 1980; Etter, 1987; Steinmann, 1994; Berger et al., 2005]. These chemical variations resulted in a corresponding variability of spectacular metamorphic assemblages that include hornblende, staurolite, kyanite, garnet, biotite, plagioclase chloritoid and zoisite/clinozoisite and which were the subject of pioneering studies on regional Barrow-type metamorphism [Chadwick, 1968; Frey, 1969,

1974, 1978; Niggli, 1970; Wenk, 1970; Fox, 1975; Livi et al., 2002]. Lower/middle amphibolite facies metamorphic conditions of 0.5–0.8 GPa and 500–550°C have been estimated for such Barrow-type metamorphism in the northeastern Lepontine dome [Engi et al., 1995; Todd and Engi, 1997; Frey and Ferreiro Máhlmann, 1999].

## 2.2. Tectonometamorphic Evolution

[9] Wiederkehr et al. [2008] showed that the metasedimentary units of the southwestern part of the investigated area (i.e., in a transect between Val Luzzzone and Pizzo Molare; Figure 1b) are characterized by a bimodal P-T path; the early HP/LT event was followed by substantial “cold” decompression and was then overprinted by late stage Barrovian amphibolite facies metamorphism (Figure 2a) [Bousquet et al., 2008; Wiederkehr et al., 2008]. Such late stage thermal overprint is totally missing in the easterly adjacent areas, i.e., east of Piz Terri and in the Engadine window (Figures 1b and 1c). There, the metasediments generally indicate greenschist facies conditions, established at more or less the same temperatures that prevailed during the earlier HP/LT event (Figure 2b) [Wiederkehr, 2009].

[10] Detailed structural and petrological investigations revealed the following tectonometamorphic evolution (Figure 2) [Wiederkehr et al., 2008]: Blueschist facies metamorphism at 350–400°C and 1.2–1.4 GPa was associated with a first deformation event D1 (Safien phase). This event is related to the formation of an accretionary wedge and subduction of the Valaisan Ocean and parts of the adjacent distal European margin. The HP/LT stage was followed by substantial isothermal or slightly cooling decompression to

**Table 1.** Summary of Investigated Samples Used for UV Laser Probe and CO<sub>2</sub> Laser Stepwise Heating Experiments<sup>a</sup>

Sample	P-T Conditions		Elevation (m)	Tectonic Unit	Mineral Assemblage	P-T Conditions <sup>b</sup>	
	X	Y				T (°C)	P (GPa)
<i>Subduction-Related Metamorphism: In Situ Laserprobe Dating Method<sup>c</sup></i>							
FOT 937	827°678	199°891	2550	Valaisan (Mundin)	Cp (fresh), WM, Chl, Qtz, Cc/Do	350–375 (1)	1.1–1.3 (1)
AlpTea 638A	829°031	198°676	2040	Valaisan (Mundin)	Cp (fresh), WM, Chl, Qtz, Cc/Do	350–375 (1)	1.1–1.3 (1)
SAF 0527	746°016	178°803	1300	Valaisan (Grava)	Cp (relic), WM, Chl, Qtz, Cc/Do	350–400 (1, 2)	1.2–1.4 (1, 2)
VAL 0580	736°871	174°310	1370	Valaisan (Grava)	Cp (relic), WM, Chl, Qtz, Cc/Do	350–400 (1, 2)	1.2–1.4 (1, 2)
<i>Collision-Related Metamorphism: In Situ Laserprobe Dating Method<sup>d</sup></i>							
LUZ 0450	716°137	157°727	1410	Valaisan (Grava)	Bt, Plag, Zo/Czo, WM, Chl, Qtz, Cc/Do	475–525 (3)	0.50–0.75 (3)
DOT 053A	713°556	155°867	2100	Valaisan (Grava)	Bt, Plag, Zo/Czo, WM, Qtz, Cc/Do	510–560 (3)	0.50–0.65 (3)
GRU 057	715°621	148°504	700	Valaisan (Grava)	Bt, Plag, WM, Qtz, Cc/Do	560–590 (3)	0.55–0.7 (3)
MOL 055	709°715	149°780	2400	Valaisan (Grava)	Bt, Plag, WM, Qtz, Cc/Do	560–590 (3)	0.6–0.8 (3)
<i>Collision-Related Metamorphism: Stepwise Heating Dating Method<sup>d</sup></i>							
LUZ 0444	716°017	157°831	1390	Valaisan (Grava)	Bt, Plag, Zo/Czo, WM, Chl, Qtz, Cc/Do	475–525 (3)	0.50–0.75 (3)
BLE 0514	715°112	155°757	1090	Valaisan (Grava)	Bt, Plag, Zo/Czo, WM, Chl, Qtz, Cc/Do	510–560 (3)	0.50–0.65 (3)
DOT 053A	713°556	155°867	2100	Valaisan (Grava)	Bt, Plag, Zo/Czo, WM, Qtz, Cc/Do	510–560 (3)	0.50–0.65 (3)
GRU 062	716°156	149°270	760	Valaisan (Grava)	Bt, Plag, WM, Qtz, Cc/Do	560–590 (3)	0.55–0.7 (3)
MOL 054	710°270	149°696	2270	Europe (Molare-Dangio)	St, Ky, Grt, Bt, Plag, WM, Qtz	560–590 (3)	0.6–0.8 (3)

<sup>a</sup>UV laser probe for white mica and biotite and CO<sub>2</sub> laser stepwise heating experiments for biotite. The sample locations are depicted in Figure 1. For each sample the precise location is given in Swiss map coordinates, elevation in meter, tectonic unit and mineral assemblage present in the investigated samples. Cp, carpholite; WM, white mica; Chl, chlorite; Qtz, quartz; Cc, calcite; Do, dolomite; Bt, biotite, Plag, plagioclase; Zo/Czo, zoisite/clinozoisite; St, staurolite; Ky, kyanite; Grt, garnet.

<sup>b</sup>Additionally estimated P-T conditions are indicated by numbers in parentheses for each sample taken from the literature: (1) *Bousquet et al.* [2002], (2) *Wiederkehr et al.* [2008], and (3) *Wiederkehr* [2009].

<sup>c</sup>Samples characterized by subduction-related HP/LT metamorphism.

<sup>d</sup>Samples characterized by collision-related Barrow-type metamorphism.

greenschist facies conditions, associated with D2 nappe stacking (Ferrera phase). This involves thrusting of HP rocks onto LP units. During D3 (Domleschg phase), representing a first nappe-refolding event, large-scale tight to isoclinal megafolds with amplitudes up to some 10 km were formed, e.g., the Lunschania antiform that can be traced in map view a long way (Figure 1b). Clearly, postdating this D3 deformation, and under static conditions at least during the initial stages, the HP/LT rocks were overprinted by regional amphibolite facies metamorphism. Temperatures progressively increase toward the west, i.e., toward the northeastern rim of the Lepontine thermal dome, from 475 to 500°C in the Val Luzzone area to 570–590°C at the Pizzo Molare and within a pressure interval of 0.6–0.7 GPa (Figure 2b). Finally, this Barrow-type metamorphism was severely overprinted by a last deformation phase D4 (Chièra phase), characterized by ductile nappe refolding and leading to the formation of the Chièra synform and the Northern Steep Belt [*Milnes*, 1974].

### 2.3. Sampling Strategy

[11] A total of 13 samples (Table 1), 12 deriving from Mesozoic metasediments (so-called “Bündnerschiefer” of the Valaisan domain) and one sample from metasediments of the distal European margin, were selected. These are well characterized with respect to the tectonometamorphic evolution outlined above. In the northeastern part of the study area, i.e., in the Valsertal and the Safiental as well as in the Engadine window (Figures 1b and 1c) where pressure-dominated metamorphism is well preserved without or with only a minor late stage thermal overprint [e.g., *Bousquet et al.*, 2002], four samples that contain white mica were collected with the aim to unravel the early, pressure-dominated meta-

morphic stage. Toward the SW, where the HP/LT metasediments were progressively overprinted by Lepontine amphibolite facies metamorphism, nine samples containing biotite were collected (see Figures 1b and 1c for locations). Note that biotite is exclusively found in these areas that experienced pervasive thermal overprint.

### 3. Experimental Procedure of <sup>40</sup>Ar/<sup>39</sup>Ar Dating

[12] The <sup>40</sup>Ar/<sup>39</sup>Ar dating was performed at the <sup>40</sup>Ar/<sup>39</sup>Ar geochronology laboratory at Potsdam University. The procedure was as follows.

#### 3.1. Sample Preparation

[13] For the in situ <sup>40</sup>Ar/<sup>39</sup>Ar UV laser probe dating technique [see, e.g., *Maluski and Monié*, 1988; *Kelley et al.*, 1994] rock sections of ~1 mm thickness and 5 mm in diameter were drilled out from sample blocks that contain the analyzed polished surface whose opposite side was used for thin section preparation. Photographs of the polished surface and corresponding thin section provided an accurate reference frame for the analyzed sections. Additionally, we performed SEM investigations of the polished sections in order to first have an accurate pattern of the distribution of both K-bearing white mica and biotite and second to have control over chemical zoning or alteration (e.g., chloritization of biotite). Both pieces of information were important for selecting the best suitable places for performing the Ar isotopic analysis. A total of eight thick sections were prepared for in situ <sup>40</sup>Ar/<sup>39</sup>Ar UV laser ablation spot analyses, four sections containing white mica and four containing biotite.

[14] For  $^{40}\text{Ar}/^{39}\text{Ar}$  dating of bulk mineral separates by the  $\text{CO}_2$  laser stepwise heating technique five hand specimens of biotite bearing mica schists were crushed and sieved. Highly enriched 250–315  $\mu\text{m}$  fractions of biotite were finally obtained by the “tapping or shaking paper method,” i.e., by spreading a small amount of sample powder on a clean sheet of paper and carefully tapping or shaking it by keeping the paper at an angle. Flat grains such as mica remain on the paper while round mineral grains roll-off. About 25 mg of biotite concentrates were further purified by handpicking under the binocular microscope. Finally, pure biotite grain separates were washed in de-ionized water within a glass beaker in an ultrasonic bath and subsequently dried in an oven at some 80° to 100°C.

### 3.2. Neutron Activation

[15] Neutron activation of polished sections and mineral separates was performed at Geesthacht Neutron Facility (GeNF), GKSS research center, Germany. Both types of samples were wrapped in Al foil and subsequently loaded into a sample container (35 mm in diameter and 43 mm in height) made of 99.999% pure Al. Finally, the sample container was wrapped in Cd foil with a thickness of 0.5 mm in order to cut off the unnecessary thermal neutron flux. Considering the smaller fast neutron flux of  $1 \times 10^{12}$  n/cm<sup>2</sup>/s compared to other research reactors, all samples were irradiated for 96 h in order to induce reactions of  $^{39}\text{K}(n, p)^{39}\text{Ar}$  in the samples. The  $^{40}\text{Ar}/^{39}\text{Ar}$  ages were obtained as a relative age against a neutron flux (J value) monitoring mineral standard, i.e., Fish Canyon tuff sanidine, which was irradiated together with samples of unknown ages. The used sanidine was prepared at the Geological Survey of Japan and its age was determined as 27.5 Ma [Uto *et al.*, 1997; Ishizuka, 1998; Ishizuka *et al.*, 2002]. This age is consistent with that of 27.51 Ma obtained by Lanphere and Baadsgaard [2001]. Additionally, crystals of  $\text{K}_2\text{SO}_4$  and  $\text{CaF}_2$  were also irradiated in order to correct the interference of Ar isotopes produced by reactions of K or Ca in the samples with neutron flux. After irradiation the samples were stored for one month at GeNF in order to cool down their activity. Finally, argon isotope analyses were performed at the  $^{40}\text{Ar}/^{39}\text{Ar}$  geochronology laboratory at Potsdam University.

### 3.3. Ar Isotopic Analysis

[16] The  $^{40}\text{Ar}/^{39}\text{Ar}$  dating system consists of (1) a Micro-mass 5400 high sensitivity–low background sector-type noble gas mass spectrometer equipped with an electron multiplier for pulse counting system which effectively works for analysis of very small amounts of gas, (2) a New Wave Research DualWave laser ablation system comprising a 50W  $\text{CO}_2$  continuous laser (10.6  $\mu\text{m}$  wavelength) and a 6 mJ UV pulsed laser (266 nm wavelength, frequency quadrupled), and (3) an ultrahigh vacuum, all-metal purification line which includes Zr-Al SAES alloy getters and a cold trap. Each analysis involves 10 min for gas extraction and purification and 15 min for data acquisition by eight cycles of peak jumping from mass 40 to mass 36. System blanks were measured after every three unknown analyses. The isotopic ratios of the investigated samples were finally obtained after

corrections of blank measurements (procedural blanks), mass discrimination by analysis of standard air Ar (atmospheric Ar), interference of the Ar isotopes derived from Ca and K by the irradiation and the decay of the radiogenic Ar isotopes ( $^{37}\text{Ar}$  and  $^{39}\text{Ar}$ ) produced by the irradiation. The final calculation of ages and errors was conducted following Uto *et al.* [1997]. The accuracy as well as the precision of the dating system was checked for every irradiation by the independent analysis of other biotite K-Ar standards, HD-B1 biotite (K-Ar age,  $24.21 \pm 0.32$  Ma) [Hess and Lippolt, 1994] and Sori93 biotite (K-Ar age,  $92.6 \pm 0.6$  Ma) [Sudo *et al.*, 1998] that are loaded together with each irradiation.

[17] The in situ  $^{40}\text{Ar}/^{39}\text{Ar}$  UV laser probe experiments generally allow for analyses characterized by highly spatial resolution [e.g., Kelley *et al.*, 1994]. Hence, the high spatial resolution of the UV laser offers the best opportunity for successful in situ dating of tiny flakes of white mica found as inclusions in quartz-calcite segregations together with preserved relics of Fe-Mg carpholite, indicative for HP/LT conditions presented in this study and documented by previous investigations [Agard *et al.*, 2002]. Generally the unknown section samples presented in this study were ablated by the UV pulse laser with the following conditions: a beam size of 35–75  $\mu\text{m}$  for white mica and 50–150  $\mu\text{m}$  for biotite, 2–4 min pulsing duration and a repetition rate of 10 Hz. Incision of the sample did not exceed 30  $\mu\text{m}$ . However, the fine-grained occurrences of the investigated white mica (in the order of a few tens of microns), together with the relatively young ages, preclude the chance of accurate direct dating by in situ laser ablation. Although the size of the laser beam is adjustable to a minimum diameter to 5  $\mu\text{m}$ , a spot size between 35 and 75  $\mu\text{m}$  for white mica and 50–150  $\mu\text{m}$  for biotite was selected in the presented study in order to generate a sufficient amount of gas which allows performing precise measurements. In the case of large biotite crystals reaching 2 mm in size, up to a maximum of 14 spots within one single biotite grain were measured. However, particularly in the case of the generally very small white mica grains (in the order of 10  $\mu\text{m}$  in size), single grain ages in the strict sense could not be obtained. In such cases the in situ  $^{40}\text{Ar}/^{39}\text{Ar}$  UV laser probe data were collected from areas within a particular fabric domain enriched in mica. However, such areas cannot be considered as exclusively consisting of mica; particularly quartz and chlorite may also have been ablated during gas extraction. In order to enhance gas production of the tiny white mica samples during laser application the analyses were generally performed along profiles (“garlands”). Consequently, the obtained apparent ages from the white mica samples do not represent single grain ages at all, but rather ages determined by integrating over a certain domain that contains ten up to a few tens of crystals, depending on the size of the white mica grains.

## 4. Sample Description and Mineral Chemistry

[18] The collected samples were studied in thin section in order to analyze the microstructure as well as for separating texturally different phengite populations. Additionally, SEM pictures were taken for selecting the best suited fabric domains for  $^{40}\text{Ar}/^{39}\text{Ar}$  investigations and also for orientation

during the in situ UV laser probe experiments. Moreover, mineral compositions of studied micas were determined by wavelength-dispersive X-ray analysis (WDS) using a CAMECA SX-100 electron microprobe at the GeoForschungsZentrum (GFZ) Potsdam. The analytical conditions included an acceleration voltage of 15 kV, a beam current of 20 nA and beam diameters of 1–10  $\mu\text{m}$ ; PAP corrections were applied. Natural and synthetic minerals were used as standards. Peak counting times were 10–20 s for major and 20–40 s for minor elements; backgrounds were counted for 5–20 s.

#### 4.1. White Mica

[19] Relics of the early HP/LT metamorphic stage are restricted to quartz-hosted fabric domains, generally found inside quartz-calcite segregations but never in the surrounding rock matrix. Therefore, all investigated white mica were picked as inclusions in quartz-calcite segregations and/or veins containing relics of Fe-Mg carpholite. This precludes the presence of detrital grains that are common in low-grade metasediments, and hence all dated white mica can be considered to be of metamorphic origin. However, white mica is stable during the entire metamorphic cycle, and hence several generations of white mica can be expected in such segregates. White mica may be found (1) associated with Fe-Mg carpholite reflecting peak pressure conditions or (2) together with chlorite as a part of the retrograde assemblage replacing carpholite, and (3) as a precursor for Fe-Mg carpholite [Agard *et al.*, 2001; Wiederkehr *et al.*, 2008]. However, these different generations of white mica can be clearly distinguished by microstructural criteria.

[20] The presence of multiple generations of white mica is also supported by electron microprobe investigations that show a significant variation of chemical composition inside this mineral group (Figure 3a). In carpholite-bearing HP/LT metasediments the Si content of phengite (Tschermak substitution) is highly pressure-sensitive [see Bousquet *et al.*, 2008, and references therein]. Maximum Si contents for mica associated with Fe-Mg carpholite vary between 3.30 and 3.40 Si per formula unit (pfu), whereas retrograde phengite associated with chlorite replacing former carpholite cluster around 3.15–3.25 Si pfu (see Figure 3a). The investigated phengites show a significantly lower interlayer content of alkalis (mainly K) in the order of 0.90–0.65 pfu, generally attributed to the incorporation of a pyrophyllite component and resulting in vacancies in the interlayer (Figure 3a) [Vidal and Parra, 2000; Bousquet *et al.*, 2002; Parra *et al.*, 2002]. Such incorporation of pyrophyllite leads to compositions of white mica that plot to the right of the celadonite to muscovite “perfect Tschermak substitution” as shown in the celadonite-pyrophyllite-muscovite triangle (Figure 3a). Hence, as is typical for low-grade HP/LT metasedimentary rocks, the composition of white mica depends on both the pyrophyllite content and Tschermak substitutions, as is shown by large deviations from the ideal Tschermak substitution in the celadonite-muscovite-pyrophyllite compositional space (Figure 3a) [Bousquet *et al.*, 2002; Parra *et al.*, 2002].

[21] Fresh Fe-Mg carpholite is only found in the Engadine window [Bousquet *et al.*, 1998, 2002], such carpholite occurrences yielded the samples AlpTea 638A and FOT 937 (see Table 1 and Figure 1c). Both samples contain large amounts of well-preserved carpholite trapped in quartz of synmetamorphic quartz-calcite veins. Most of the white mica is associated with chlorite forming needle-shaped aggregates that partially or completely replace Fe-Mg carpholite crystals. Hence, white mica found inside such pseudomorphs after carpholite are unambiguously related to the retrograde evolution. But additionally, some rare white mica flakes were found to be closely associated with carpholite, precluding a retrograde formation because the surrounding quartz grain did not recrystallize into subgrains after trapping of carpholite and phengite. Hence, such isolated white mica can be related to HP/LT conditions and most likely represent a relic of peak pressure white mica [see also Bousquet *et al.*, 1998]. The coexistence of retrograde phengite with relics of peak pressure phengite is also documented by the significant chemical variations found in the Engadine window (Figure 3a).

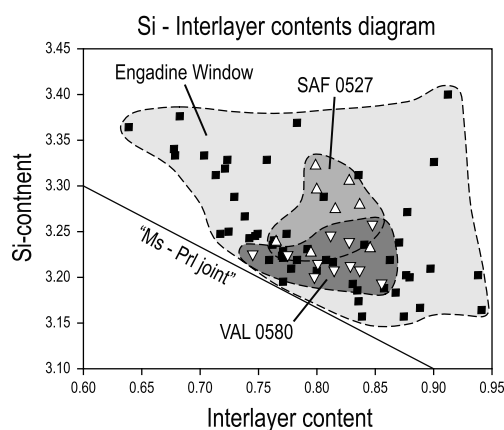
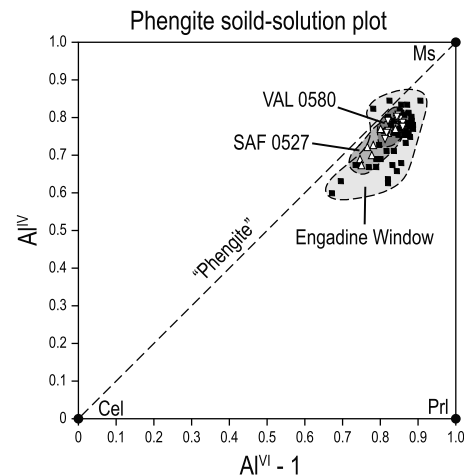
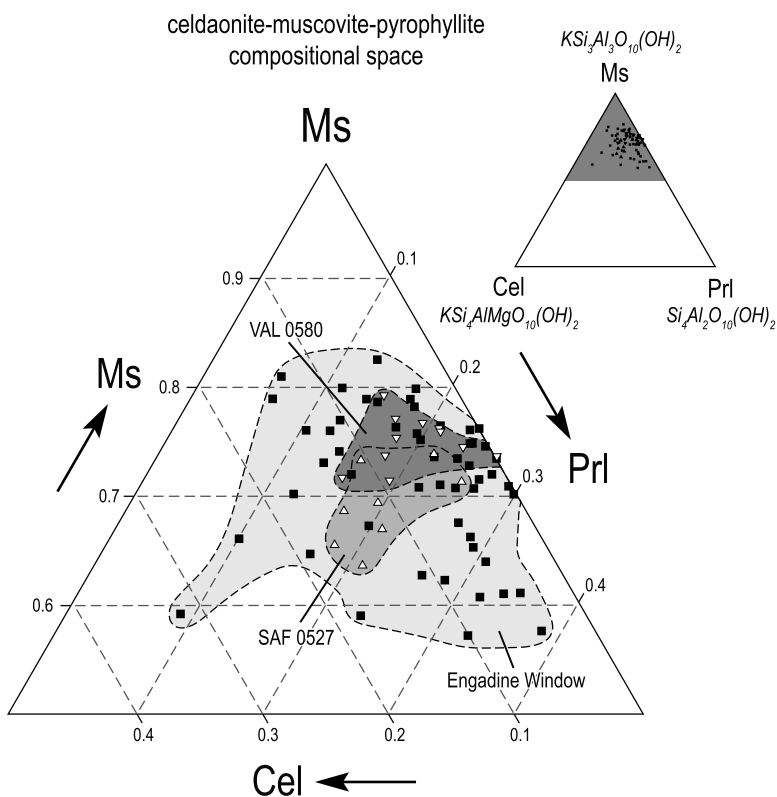
[22] Further to the west, Fe-Mg carpholite is considerably less well preserved. In general it is partially or completely replaced by white mica and chlorite, and only some relics of carpholite could be found as quartz-hosted, hair-like fibers [Bousquet *et al.*, 2002; Wiederkehr *et al.*, 2008]. Sample SAF 0527 (Table 1 and Figure 1b) from the northern Safiental is similar to the samples from the Engadine window in that it shows the same textural features described above. However, a considerably stronger retrogression is observed in SAF 0527, as is documented by recrystallization of the surrounding quartz into subgrains; also tiny relics of carpholite and associated white mica are only found locally in older grains that escaped recrystallization. Again, needle-shaped aggregates of white mica and chlorite, interpreted as pseudomorphs after carpholite, are found to completely replace Fe-Mg carpholite. The chemical composition of the investigated phengites is significantly more homogeneous than in the Engadine window; Si contents are between 3.20 and 3.35 pfu and an interlayer content of 0.75–0.85 pfu is determined (Figure 3a).

[23] Sample VAL 0580, collected in the eastern area of Valsertal (Table 1 and Figure 1b) is totally different from the above described investigated samples. It is characterized by large areas consisting of white mica and chlorite, oriented parallel to the main foliation surrounding several relic quartz grains within which tiny fibers of carpholite are still preserved. The chemical composition of the white mica is rather uniform, showing a maximum Si content 3.20–3.25 pfu and an interlayer content between 0.75 and 0.85 pfu (Figure 3a). This rather uniform white mica composition points toward a pervasive retrogression and associated recrystallization of the earlier HP/LT stage.

[24] In summary white mica may occur within at least the following three texturally distinguishable associations:

[25] 1. Completely isolated white mica flakes are entrapped in quartz grains that also contain preserved relics of Fe-Mg carpholite, indicating that both white mica and carpholite formed under the same conditions, i.e., during HP/LT metamorphism.

a) White mica composition



b) Biotite composition

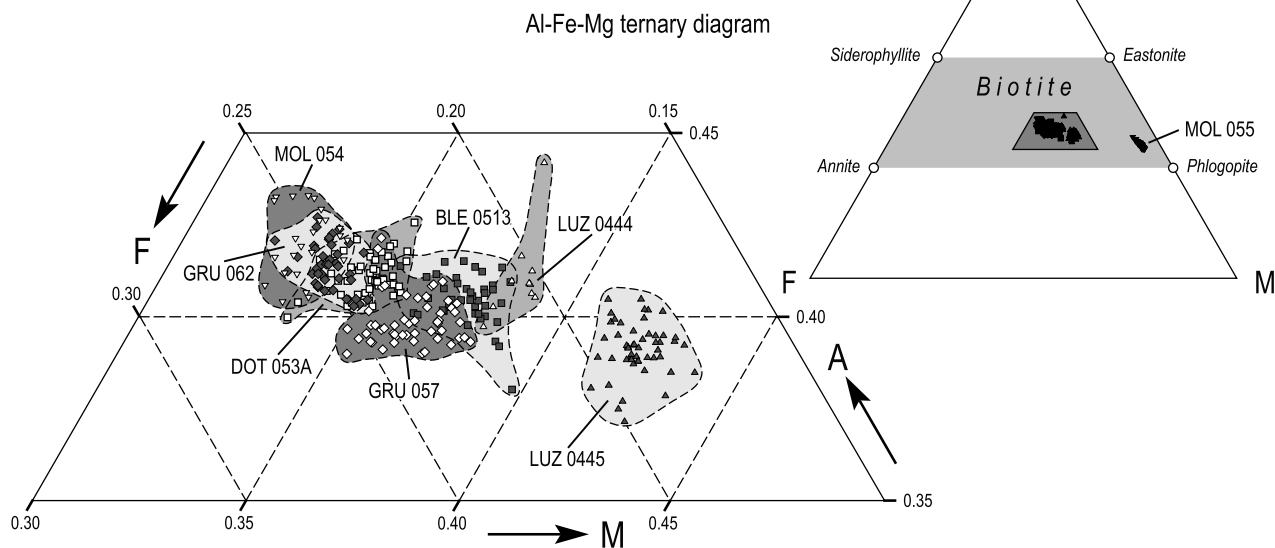


**Figure 3.** Chemical composition of mica used for  $^{40}\text{Ar}/^{39}\text{Ar}$  isotopic analysis. (a) White mica compositions determined by electron microprobe analysis, presented in celadonite-muscovite-pyrophyllite compositional space, in a phengite solid solution graph, and in a Si content versus interlayer content diagram, respectively. (b) Al-Fe-Mg ternary diagram showing the chemical composition of the biotite samples.

[26] 2. White mica intimately associated with chlorite forms needle-shaped aggregates entrapped in quartz grains, replacing Fe-Mg carpholite. Such mineral associations and their characteristic needle-shaped habit are interpreted to represent pseudomorphs after carpholite and are therefore related to the retrograde metamorphic evolution; that is, they formed during decompression immediately after the peak pressure stage.

[27] 3. White mica associated with chlorite, oriented parallel to the main foliation, forms large irregular shaped areas surrounding tiny quartz grains may still contain some relics of Fe-Mg carpholite. This type of white mica was analyzed only in the case of sample VAL 0580.

#### 4.2. Biotite

[28] Biotite was only found in the southwest (southern Lukmanier area and Pizzo Molare; Figure 1b) where the Barrovian overprint reached lower/middle amphibolite facies conditions. A total of eight samples were selected for  $^{40}\text{Ar}/^{39}\text{Ar}$  investigations, sample DOT 043A has been investigated using both stepwise heating and in situ laser probe dating (see Table 1 and Figure 1b). Except for sample MOL 055, all investigated biotite samples are characterized by a rather uniform chemical composition clustering around intermediate XMg values slightly shifted toward phlogopite (Figure 3b). Sample LUZ 0445 is significantly shifted away from this cluster and shows a slightly higher Mg content. Sample MOL 055 is characterized by an Mg content that almost represents phlogopite (Figure 3b). Within a given sample the chemical composition of biotite was rather homogeneous, within core and rim of a given grain as well as between different grains. This low variation in chemical composition supports the interpretation that biotite formed as the result of a single metamorphic event, i.e., Barrow-type thermal overprint. This contrasts with the wide range of chemical composition in the investigated white micas that indicates the coexistence of several generations of white mica reflecting various stages established along the early metamorphic evolution, i.e., during the subduction-related HP/LT event and subsequent decompression, including greenschist facies overprint.

[29] Biotite generally occurs as big flakes, up to a few mm in size, oriented parallel or across the main foliation. Particularly, the widespread occurrences of biotite that grew across the main foliation (so-called “Querbiotit”) document late stage (post-D3) formation. Seven investigated biotite samples were collected from Valaisan-derived calcschists that are generally characterized by the mineral assemblage biotite – plagioclase – zoisite/clinozoisite – phengite – quartz – calcite/dolomite  $\pm$  chlorite  $\pm$  titanite. Only sample MOL 054 from a staurolite – kyanite – garnet bearing micaschist,

belonging to metasedimentary cover units of the distal European margin, shows a completely different mineralogical composition (Table 1 and Figure 1b). Although all biotite samples were carefully selected and checked for freshness to avoid problems resulting from retrogression and alteration, chloritization of biotite is present in all investigated samples and includes chlorite lamellae within biotite [see also *Clauer*, 1980; *Clauer et al.*, 1982; *Jeong et al.*, 2006; *Allaz*, 2008]. To reduce the influence of chloritization as much as possible, the grain separates were purified with careful check by hand picking. Furthermore, the rock sections were investigated under the SEM prior to in situ  $^{40}\text{Ar}/^{39}\text{Ar}$  laser probe dating.

### 5. Results of the $^{40}\text{Ar}/^{39}\text{Ar}$ Measurements

[30] We first present the results of in situ laser probe experiments on white mica and biotite, followed by the results of stepwise heating investigations on biotite. All recorded in situ ages are depicted in Figures 4, 5, and 6 on SEM images, allowing for identification of the relationships between apparent ages and the location of the dated crystal domains in the microstructural context. All the results of the in situ laser probe experiments and the stepwise heating experiments are listed in Tables 2, 3, and 4, respectively. All isotopic ages and calculated weighted averages are quoted with their  $1\sigma$  uncertainties; error on single ages does not include the uncertainty in the J value.

#### 5.1. In Situ $^{40}\text{Ar}/^{39}\text{Ar}$ UV Laser Probe Ages on White Mica

##### 5.1.1. Samples AlpTea 638A and FOT 937 (Engadine Window)

[31] Sample AlpTea 638A (Figure 4a) contains a large, irregularly shaped aggregate consisting of white mica and chlorite, as well as numerous tiny and isolated carpholite needles and phengite flakes in the immediate vicinity (Figures 4b, 4d, and 4e). The microstructure of sample FOT 937 is dominated by numerous needle-shaped phengite-chlorite aggregates, replacing former Fe-Mg carpholite crystals (Figures 4f, 4g, and 4h) and interpreted as pseudomorphs after carpholite. The white mica in both samples yield ages that scatter between  $45.82 \pm 5.05$  and  $28.92 \pm 1.38$  Ma (Figure 4 and Table 2). Phengite that is closely associated with chlorite yields rather precise and consistent ages in the time interval 29.14–32.25 Ma in the case of sample AlpTea 638A (Figure 4c), and between 31.24–28.92 Ma in the case of sample FOT 937 (Figure 4g). However, it was found that tiny phengite flakes, more or less isolated and entrapped in quartz, yield older ages between  $43.64 \pm 8.85$  and  $37.08 \pm 4.06$  Ma (Figures 4b, 4d, and 4e). Ages around 40 Ma or more were also recorded within a minor portion of domains

**Figure 4.** SEM backscattered electron photomicrographs of carpholite-bearing synmetamorphic quartz-calcite segregations and location of the domains analyzed by laser ablation in white mica. Errors are  $1\sigma$  and do not include the uncertainty in the J value. Mineral abbreviations used: Qtz, quartz; WM, white mica; Chl, chlorite; Cp, Fe-Mg carpholite. (a) Overview of the characteristic microstructure of sample AlpTea 638A; dashed lines denote outlines of Figures 4b, 4c and 4d. (b–e) Locations of traces ablated during laser experiments as well as the obtained apparent ages on white mica in sample AlpTea 638A. (f) Overview of the microstructure of sample FOT 937; dashed lines denote outlines of Figures 4g and 4h. (g and h) Locations of traces ablated during laser experiments as well as the obtained apparent ages on white mica in sample FOT 937.

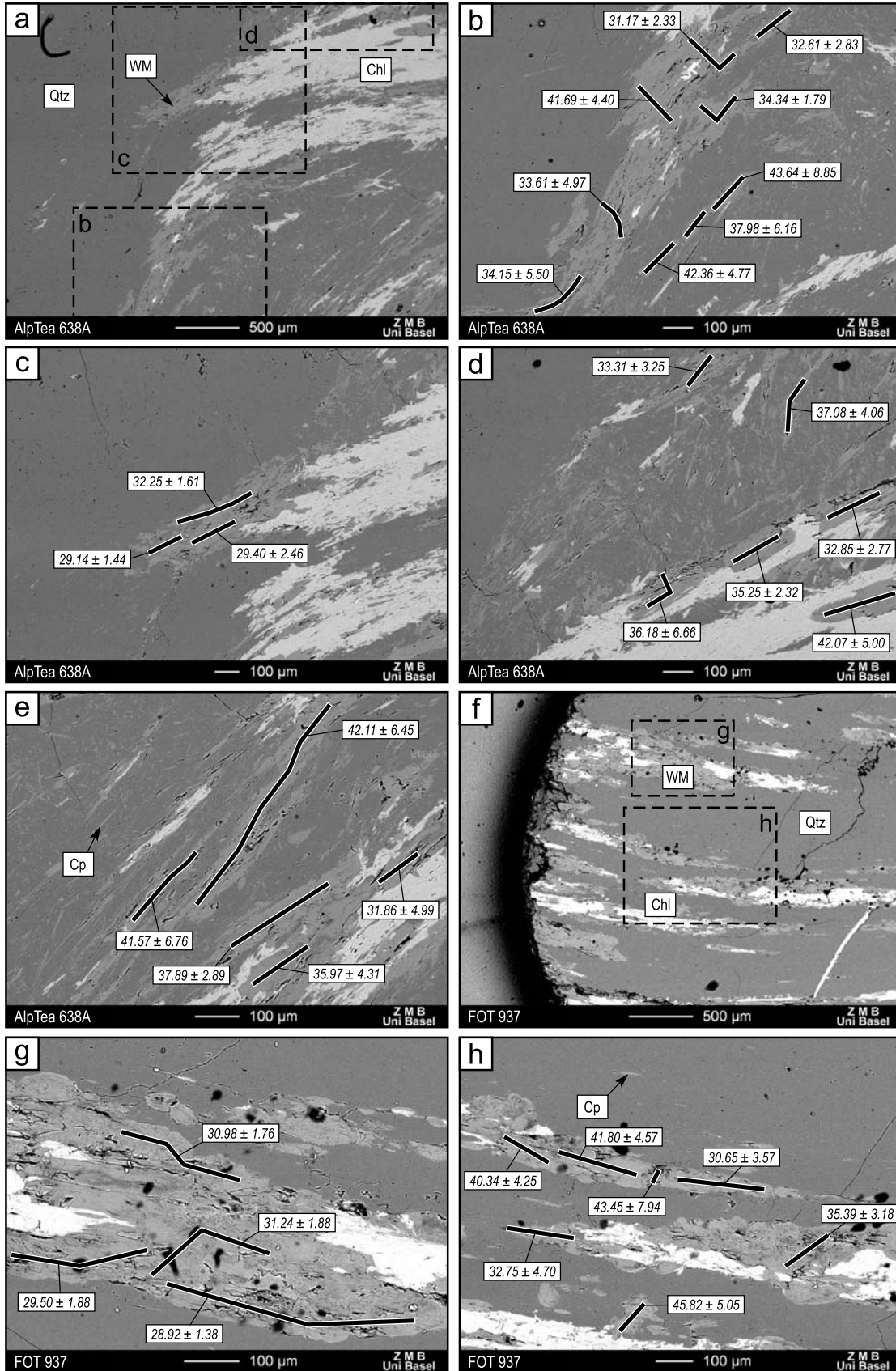


Figure 4

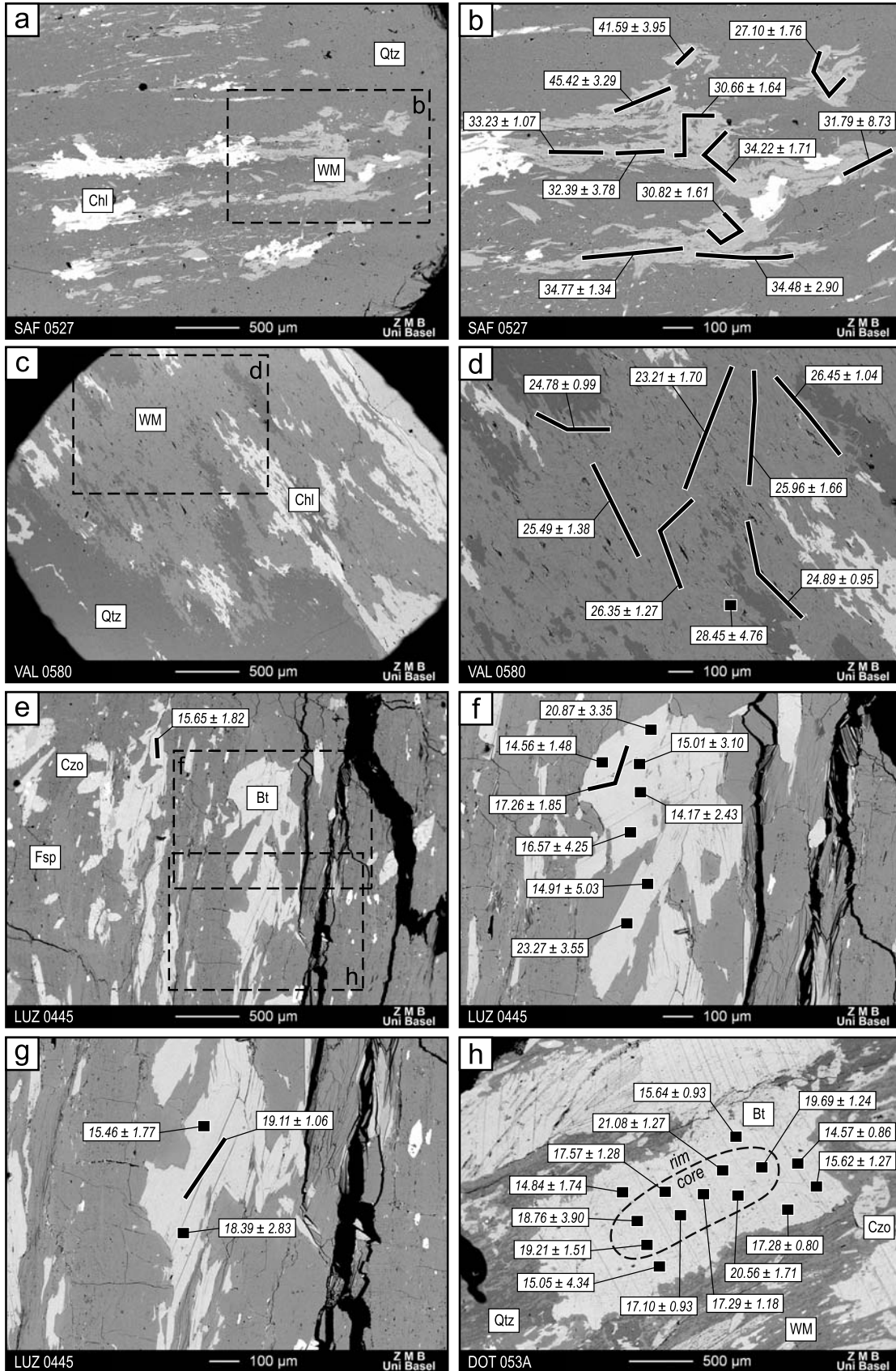


Figure 5

that are well inside or close to phengite-chlorite aggregates (Figures 4b and 4d), as well as inside chlorite-phengite associations that are interpreted to have replaced carpholite (Figure 4h). An intermediate range of ages was found inside phengite-chlorite assemblages (Figures 4b, 4d, 4e, and 4h), scattering between 36.18 and 32.75 Ma, i.e., an age range bracketed by the pre-40 Ma ages and the well-defined age population around 30 Ma.

### 5.1.2. Sample SAF 0527 (Safiental)

[32] The microstructure of sample SAF 0527 is characterized by an irregularly shaped aggregate of white mica and chlorite fully entrapped in quartz. Phengite occurs as flower-like nuclei or as numerous tiny flakes (Figures 5a and 5b). In some places white mica is intimately associated with chlorite. In the immediate vicinity numerous tiny quartz-hosted relics of carpholite needles also occur, being significantly less frequent and generally less preserved in comparison to the samples from the Engadine window. However, the recorded  $^{40}\text{Ar}/^{39}\text{Ar}$  ages fall into exactly the same range as those from the Engadine window. They scatter between  $45.42 \pm 3.29$  and  $27.10 \pm 1.76$  Ma, most ages being found within the 35–31 Ma time interval (Figures 5b and Table 2). No obvious trend between the obtained ages and their location in the microstructure is possible.

### 5.1.3. Sample VAL 0580 (Valsertal)

[33] A completely different microstructure compared to the samples from the Engadine window and Safiental characterizes sample VAL 0580 (Figure 5c). White mica occurs as large aggregates oriented parallel to the main foliation and is intimately associated with chlorite; carpholite is only found as tiny quartz-hosted needles and restricted to relic quartz grains which are dispersedly distributed within the main foliation. The  $^{40}\text{Ar}/^{39}\text{Ar}$  ages are well defined and consistently between  $23.21 \pm 1.70$  and  $28.45 \pm 4.76$  Ma (Figure 5d and Table 2), the weighted average age yields  $25.40 \pm 0.45$  Ma. Hence, significantly lower ages are found in sample VAL 0580 compared to the other samples described before. Moreover, such uniform and consistent ages point toward the presence of one distinct generation of phengite (see later discussion).

## 5.2. In Situ $^{40}\text{Ar}/^{39}\text{Ar}$ UV Laser Probe Ages of Biotite

[34] The results from four biotite-bearing samples investigated by the in situ  $^{40}\text{Ar}/^{39}\text{Ar}$  UV laser probe dating tech-

nique will be briefly presented in order of increasing temperatures related to Barrovian overprint. The four samples occur between a location coinciding with the first biotite occurrence in Val Luzzone (LUZ 0445) and the maximum temperature area around Pizzo Molare (MOL 055; Figure 1b and Table 1). All investigated biotite grains were very much larger compared to the analyzed white micas, which allows for numerous single spot analyses per grain. Hence, the measured biotite ages typically represent single grain ages. Nevertheless, larger areas were occasionally ablated along profiles in order to enhance the amount of gas.

[35] In sample LUZ 0445 biotite grains or aggregates are found completely contained within large plagioclase porphyroblasts (Figure 5e). Plagioclase also encloses numerous zoisite/clinozoisite grains and occasionally white mica. Typically, biotite, plagioclase and zoisite/clinozoisite are seen to have formed when temperatures increased during the late stage Barrow-type thermal overprint [Wiederkehr *et al.*, 2008]. All recorded biotite ages scatter between  $23.27 \pm 3.55$  and  $14.17 \pm 2.43$  Ma (Table 3). No obvious correlation between age and microstructural position could be detected (Figures 5e, 5f, and 5g). A weighted average age of  $17.05 \pm 0.59$  Ma was calculated for this sample (see Figure 7a).

[36] Within sample DOT 053A we investigated a ca. 2 mm long and 1 mm wide biotite grain that grew across the main foliation (typical “Querbiotit”; Figure 5h). Given the large grain size the laser spot was opened up to a diameter of 150  $\mu\text{m}$ . The obtained ages are bracket between  $21.08 \pm 1.27$  and  $14.57 \pm 0.86$  Ma (Table 3). Older ages are generally found in the core of the grain and cluster between 21 and 17 Ma; toward the rim the ages tend to be slightly younger and vary between 17 and 15 Ma (Figure 5h). This core-rim age relation is significant at the  $2\sigma$  confidence level and a weighted average age of  $18.58 \pm 0.47$  Ma was calculated for the core and  $15.80 \pm 0.44$  Ma for the rim, respectively (Figure 7b).

[37] Sample GRU 057 contains fine-grained biotite flakes that are oriented parallel to the only weakly developed main foliation and that are dispersedly distributed within a matrix mainly formed by calcite/dolomite with some minor amount of quartz (Figures 6a and 6c). Due to the relatively small grain size (around 100  $\mu\text{m}$ ) it was possible to obtain more than one age per grain only in rare cases. Also, the extracted amount of gas was significantly lower, which results in larger uncertainties. In comparison to the other investigated samples the

**Figure 5.** SEM backscattered electron photomicrographs of investigated white mica- and biotite-bearing samples and location of the domains analyzed by laser ablation in white mica or biotite. Errors are  $1\sigma$  and do not include the uncertainty in the J value. Mineral abbreviations used: Qtz, quartz; WM, white mica; Chl, chlorite; Bt, biotite; Czo, clinozoisite; Fsp, feldspar (plagioclase). (a) Overview of the microstructure of sample SAF 0527; dashed lines denote outlines of Figure 5b. (b) Microstructural details of the same sample showing the location of the traces ablated during laser experiments and the apparent ages obtained on white mica. (c) General overview of the microstructure of sample VAL 0580; note the significantly different microstructure compared to the other mica samples, phengite, and chlorite being oriented parallel to the main foliation. Dashed lines denote outlines of Figure 5d. (d) Microstructural details within sample VAL 0580 and location of ablated points or traces and apparent ages obtained for white mica. (e) General overview of the microstructure of sample LUZ 0445 within which biotite grains were investigated; dashed lines denote outlines of Figures 5f and 5g. (f and g) Details of the microstructure of sample LUZ 0445 and location of ablated points or traces and apparent ages obtained for biotite. (h) Biotite flake growing across the main foliation (“Querbiotit”) in sample DOT 053A and location of ablated points and apparent ages obtained for biotite.

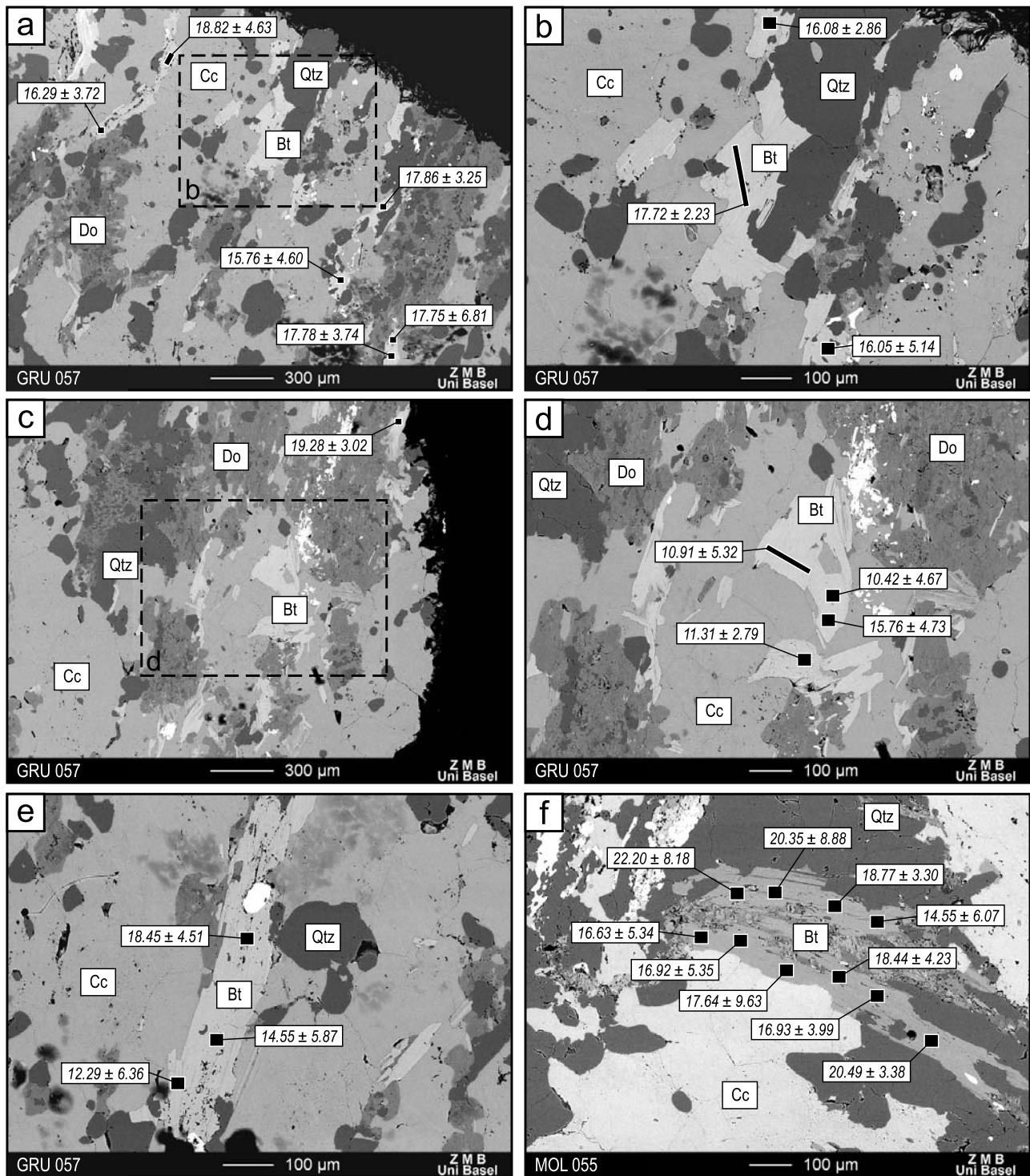


**Figure 6.** SEM backscattered electron photomicrographs of investigated biotite-bearing samples and location of the domains analyzed by laser ablation in biotite. Errors are  $1\sigma$  and do not include the uncertainty in the J value. Mineral abbreviations used: Qtz, quartz; Bt, biotite; Cc, calcite; Do, dolomite. (a–e) Location of points and traces ablated and apparent ages obtained within sample GRU 057. The dashed rectangles denote the positions of the details shown in Figures 6b and 6d, respectively. (f) Biotite flake in sample MOL 055 and locations of ablated points and apparent ages obtained for biotite.

**Table 2.** Full Results of White Mica  $^{40}\text{Ar}/^{39}\text{Ar}$  in Situ UV Laser Probe Analysis<sup>a</sup>

Run ID	$^{40}\text{Ar}/^{39}\text{Ar}$	$^{38}\text{Ar}/^{39}\text{Ar}$	$^{37}\text{Ar}/^{39}\text{Ar}$	$^{36}\text{Ar}/^{39}\text{Ar} (\times 10^{-3})$	$^{40}\text{Ar}^*$ (%)	$^{40}\text{Ar}^*/^{39}\text{Ar}_K$	Age $\pm 1\sigma$ (Ma)
<i>Sample AlpTea 938A (J = 0.001973)</i>							
U0800601	14.111 $\pm$ 0.157	0.015 $\pm$ 0.002	0.017 $\pm$ 0.033	19.256 $\pm$ 2.357	59.7	8.423 $\pm$ 0.710	29.7 $\pm$ 2.5
U0800605	32.281 $\pm$ 0.162	0.033 $\pm$ 0.001	0.016 $\pm$ 0.028	76.289 $\pm$ 1.694	30.2	9.739 $\pm$ 0.511	34.3 $\pm$ 1.8
U0800607	16.485 $\pm$ 0.163	0.017 $\pm$ 0.002	0.024 $\pm$ 0.037	24.517 $\pm$ 2.692	56.1	9.244 $\pm$ 0.810	32.6 $\pm$ 2.8
U0800608	68.080 $\pm$ 0.790	0.052 $\pm$ 0.004	0.082 $\pm$ 0.149	189.919 $\pm$ 6.376	17.6	11.970 $\pm$ 1.853	42.1 $\pm$ 6.4
U0800609	43.290 $\pm$ 1.096	0.032 $\pm$ 0.007	0.066 $\pm$ 0.054	106.550 $\pm$ 6.818	27.3	11.814 $\pm$ 1.944	41.6 $\pm$ 6.8
U0800610	20.840 $\pm$ 0.303	0.023 $\pm$ 0.003	0.033 $\pm$ 0.049	34.133 $\pm$ 2.679	51.6	10.758 $\pm$ 0.828	37.9 $\pm$ 2.9
U0800611	21.801 $\pm$ 0.208	0.027 $\pm$ 0.002	0.019 $\pm$ 0.017	39.945 $\pm$ 2.169	45.9	9.999 $\pm$ 0.662	35.2 $\pm$ 2.3
U0800612	32.100 $\pm$ 0.334	0.035 $\pm$ 0.005	0.033 $\pm$ 0.026	73.027 $\pm$ 3.892	32.8	10.525 $\pm$ 1.164	37.1 $\pm$ 4.1
U0800613	33.619 $\pm$ 0.359	0.033 $\pm$ 0.004	0.015 $\pm$ 0.058	81.810 $\pm$ 3.056	28.1	9.446 $\pm$ 0.928	33.3 $\pm$ 3.2
U0800614	12.117 $\pm$ 0.138	0.016 $\pm$ 0.002	0.013 $\pm$ 0.022	13.083 $\pm$ 1.340	68.1	8.252 $\pm$ 0.409	29.1 $\pm$ 1.4
U0800615	12.519 $\pm$ 0.114	0.017 $\pm$ 0.002	0.010 $\pm$ 0.021	11.437 $\pm$ 1.521	73.0	9.141 $\pm$ 0.460	32.2 $\pm$ 1.6
U0800616	26.911 $\pm$ 0.339	0.028 $\pm$ 0.004	0.040 $\pm$ 0.061	50.990 $\pm$ 4.273	44.0	11.848 $\pm$ 1.264	41.7 $\pm$ 4.4
U0800617	15.617 $\pm$ 0.177	0.022 $\pm$ 0.003	0.036 $\pm$ 0.052	20.616 $\pm$ 4.788	61.0	9.530 $\pm$ 1.421	33.6 $\pm$ 5.0
U0800618	18.063 $\pm$ 0.188	0.024 $\pm$ 0.004	0.040 $\pm$ 0.057	28.368 $\pm$ 5.315	53.6	9.685 $\pm$ 1.575	34.1 $\pm$ 5.5
U0800619	40.272 $\pm$ 0.737	0.038 $\pm$ 0.006	0.068 $\pm$ 0.089	94.320 $\pm$ 8.685	30.8	12.409 $\pm$ 2.547	43.6 $\pm$ 8.9
U0800620	31.637 $\pm$ 0.546	0.029 $\pm$ 0.006	0.050 $\pm$ 0.056	70.599 $\pm$ 6.025	34.1	10.782 $\pm$ 1.767	38.0 $\pm$ 6.2
U0800621	19.130 $\pm$ 0.384	0.022 $\pm$ 0.005	0.054 $\pm$ 0.078	24.008 $\pm$ 4.563	62.9	12.043 $\pm$ 1.370	42.4 $\pm$ 4.8
U0800622	15.692 $\pm$ 0.164	0.020 $\pm$ 0.002	0.025 $\pm$ 0.040	23.223 $\pm$ 2.218	56.3	8.832 $\pm$ 0.665	31.2 $\pm$ 2.3
U0800623	16.055 $\pm$ 0.244	0.020 $\pm$ 0.003	0.087 $\pm$ 0.075	19.824 $\pm$ 4.129	63.6	10.208 $\pm$ 1.234	36.0 $\pm$ 4.3
U0800624	16.647 $\pm$ 0.297	0.017 $\pm$ 0.005	0.036 $\pm$ 0.058	25.787 $\pm$ 4.780	54.3	9.031 $\pm$ 1.426	31.9 $\pm$ 5.0
U0800627	18.363 $\pm$ 0.176	0.028 $\pm$ 0.004	0.088 $\pm$ 0.076	21.714 $\pm$ 4.839	65.1	11.958 $\pm$ 1.437	42.1 $\pm$ 5.0
U0800628	15.336 $\pm$ 0.158	0.021 $\pm$ 0.003	0.097 $\pm$ 0.034	20.424 $\pm$ 2.647	60.7	9.314 $\pm$ 0.790	32.9 $\pm$ 2.8
U0800629	22.969 $\pm$ 0.343	0.033 $\pm$ 0.004	0.135 $\pm$ 0.070	43.048 $\pm$ 6.389	44.7	10.266 $\pm$ 1.908	36.2 $\pm$ 6.7
<i>Sample FOT 937 (J = 0.001975)</i>							
U0800801	16.184 $\pm$ 0.090	0.024 $\pm$ 0.001	0.029 $\pm$ 0.036	27.097 $\pm$ 1.308	50.5	8.181 $\pm$ 0.392	28.9 $\pm$ 1.4
U0800802	15.167 $\pm$ 0.114	0.021 $\pm$ 0.002	0.002 $\pm$ 0.030	21.652 $\pm$ 1.674	57.8	8.769 $\pm$ 0.500	31.0 $\pm$ 1.8
U0800804	23.329 $\pm$ 0.155	0.027 $\pm$ 0.002	0.014 $\pm$ 0.038	50.705 $\pm$ 1.796	35.8	8.348 $\pm$ 0.535	29.5 $\pm$ 1.9
U0800805	19.363 $\pm$ 0.170	0.024 $\pm$ 0.003	0.025 $\pm$ 0.034	35.608 $\pm$ 1.779	45.7	8.844 $\pm$ 0.535	31.2 $\pm$ 1.9
U0800809	21.225 $\pm$ 0.368	0.025 $\pm$ 0.004	0.048 $\pm$ 0.084	31.689 $\pm$ 4.310	55.9	11.867 $\pm$ 1.312	41.8 $\pm$ 4.6
U0800810	18.752 $\pm$ 0.195	0.023 $\pm$ 0.002	0.016 $\pm$ 0.054	34.102 $\pm$ 3.407	46.3	8.677 $\pm$ 1.018	30.7 $\pm$ 3.6
U0800811	17.367 $\pm$ 0.353	0.028 $\pm$ 0.004	0.059 $\pm$ 0.046	27.408 $\pm$ 4.410	53.4	9.276 $\pm$ 1.344	32.8 $\pm$ 4.7
U0800814	19.031 $\pm$ 0.441	0.025 $\pm$ 0.003	0.032 $\pm$ 0.082	30.478 $\pm$ 2.810	52.7	10.029 $\pm$ 0.909	35.4 $\pm$ 3.2
U0800816	20.978 $\pm$ 0.553	0.014 $\pm$ 0.004	0.061 $\pm$ 0.081	32.280 $\pm$ 3.751	54.6	11.448 $\pm$ 1.218	40.3 $\pm$ 4.2
U0800817	21.529 $\pm$ 0.700	0.025 $\pm$ 0.004	0.069 $\pm$ 0.118	31.118 $\pm$ 7.397	57.3	12.343 $\pm$ 2.282	43.5 $\pm$ 7.9
U0800818	20.241 $\pm$ 0.666	0.025 $\pm$ 0.003	0.078 $\pm$ 0.145	24.457 $\pm$ 4.547	64.3	13.025 $\pm$ 1.453	45.8 $\pm$ 5.1
<i>Sample SAF 0527 (J = 0.001970)</i>							
U0801102	60.570 $\pm$ 0.809	0.049 $\pm$ 0.003	0.041 $\pm$ 0.083	161.195 $\pm$ 3.709	21.4	12.943 $\pm$ 0.948	45.4 $\pm$ 3.3
U0801103	15.866 $\pm$ 0.113	0.019 $\pm$ 0.001	0.009 $\pm$ 0.021	21.764 $\pm$ 0.997	59.5	9.436 $\pm$ 0.304	33.2 $\pm$ 1.1
U0801104	20.927 $\pm$ 0.325	0.025 $\pm$ 0.003	0.040 $\pm$ 0.048	39.721 $\pm$ 3.601	43.9	9.195 $\pm$ 1.083	32.4 $\pm$ 3.8
U0801105	11.371 $\pm$ 0.139	0.020 $\pm$ 0.002	0.013 $\pm$ 0.020	9.046 $\pm$ 1.535	76.5	8.699 $\pm$ 0.468	30.7 $\pm$ 1.6
U0801106	29.132 $\pm$ 0.222	0.031 $\pm$ 0.002	0.004 $\pm$ 0.024	72.585 $\pm$ 1.759	26.4	7.684 $\pm$ 0.501	27.1 $\pm$ 1.8
U0801107	12.044 $\pm$ 0.076	0.018 $\pm$ 0.001	0.011 $\pm$ 0.015	11.161 $\pm$ 1.536	72.6	8.748 $\pm$ 0.459	30.8 $\pm$ 1.6
U0801108	22.386 $\pm$ 0.172	0.026 $\pm$ 0.002	0.055 $\pm$ 0.044	42.639 $\pm$ 2.801	43.7	9.794 $\pm$ 0.830	34.5 $\pm$ 2.9
U0801109	14.647 $\pm$ 0.102	0.016 $\pm$ 0.001	0.013 $\pm$ 0.012	16.143 $\pm$ 1.273	67.4	9.878 $\pm$ 0.383	34.8 $\pm$ 1.3
U0801110	11.712 $\pm$ 0.204	0.019 $\pm$ 0.001	0.004 $\pm$ 0.035	6.744 $\pm$ 1.520	83.0	9.720 $\pm$ 0.488	34.2 $\pm$ 1.7
U0801111	26.547 $\pm$ 0.326	0.026 $\pm$ 0.002	0.072 $\pm$ 0.049	49.810 $\pm$ 3.747	44.6	11.838 $\pm$ 1.136	41.6 $\pm$ 3.9
U0801112	19.664 $\pm$ 0.653	0.022 $\pm$ 0.006	0.010 $\pm$ 0.094	36.014 $\pm$ 8.196	45.9	9.023 $\pm$ 2.500	31.8 $\pm$ 8.7
<i>Sample VAL 0580 (J = 0.001959)</i>							
U0801001	9.325 $\pm$ 0.085	0.019 $\pm$ 0.001	0.012 $\pm$ 0.016	6.254 $\pm$ 1.192	80.2	7.479 $\pm$ 0.361	26.4 $\pm$ 1.3
U0801002	8.875 $\pm$ 0.081	0.018 $\pm$ 0.001	0.004 $\pm$ 0.014	6.132 $\pm$ 0.882	79.6	7.063 $\pm$ 0.271	24.9 $\pm$ 1.0
U0801003	10.305 $\pm$ 0.084	0.018 $\pm$ 0.002	0.002 $\pm$ 0.026	9.462 $\pm$ 0.970	72.9	7.509 $\pm$ 0.296	26.5 $\pm$ 1.0
U0801004	10.541 $\pm$ 0.279	0.021 $\pm$ 0.002	0.011 $\pm$ 0.022	13.402 $\pm$ 1.395	62.4	6.582 $\pm$ 0.484	23.2 $\pm$ 1.7
U0801005	9.962 $\pm$ 0.113	0.019 $\pm$ 0.001	0.002 $\pm$ 0.035	8.775 $\pm$ 1.564	74.0	7.370 $\pm$ 0.474	26.0 $\pm$ 1.7
U0801006	8.963 $\pm$ 0.208	0.018 $\pm$ 0.001	0.012 $\pm$ 0.014	6.541 $\pm$ 0.682	78.5	7.032 $\pm$ 0.282	24.8 $\pm$ 1.0
U0801007	9.345 $\pm$ 0.183	0.016 $\pm$ 0.001	0.009 $\pm$ 0.014	7.150 $\pm$ 1.199	77.4	7.233 $\pm$ 0.394	25.5 $\pm$ 1.4
U0801008	10.417 $\pm$ 0.412	0.016 $\pm$ 0.003	0.039 $\pm$ 0.076	7.919 $\pm$ 4.411	77.6	8.082 $\pm$ 1.363	28.5 $\pm$ 4.8

<sup>a</sup>Uncertainties are given in  $1\sigma$ ; error on single ages does not include the uncertainty in the J value.

recorded ages of GRU 057, representing a population of single grain ages, show a larger scatter; most ages cluster in the 18–16 Ma time interval (Figures 6a–6e and Table 3), the weighted average age is  $16.11 \pm 0.92$  Ma (Figure 7c).

[38] Within sample MOL 055 a total of 10 ages was obtained from one single flake of biotite, approximately

0.75 mm long and 0.3 mm wide, embedded in a matrix consisting of quartz and calcite/dolomite (Figure 6f). Since we used a small laser spot size, varying between 50 and  $75 \mu\text{m}$ , only small amounts of gas were extracted which results in high uncertainties. The recorded ages between  $22.20 \pm 8.18$  and  $14.55 \pm 6.07$  Ma (Figure 6f and Table 3)

**Table 3.** Full Results of Biotite  $^{40}\text{Ar}/^{39}\text{Ar}$  in Situ UV Laser Stepwise Heating Analysis<sup>a</sup>

Run ID	$^{40}\text{Ar}/^{39}\text{Ar}$	$^{38}\text{Ar}/^{39}\text{Ar}$	$^{37}\text{Ar}/^{39}\text{Ar}$	$^{36}\text{Ar}/^{39}\text{Ar} (\times 10^{-3})$	$^{40}\text{Ar}^*$ (%)	$^{40}\text{Ar}^*/^{39}\text{Ar}_K$	Age (Ma) $\pm 1\sigma$
<i>Sample LUZ 0450 (J = 0.001984)</i>							
U0800408	28.281 $\pm$ 0.357	0.028 $\pm$ 0.002	0.011 $\pm$ 0.016	81.890 $\pm$ 1.370	14.4	4.084 $\pm$ 0.417	14.6 $\pm$ 1.5
U0800409	45.208 $\pm$ 0.421	0.046 $\pm$ 0.004	0.163 $\pm$ 0.059	133.209 $\pm$ 3.265	13.0	5.866 $\pm$ 0.947	20.9 $\pm$ 3.4
U0800410	17.502 $\pm$ 0.212	0.026 $\pm$ 0.002	0.093 $\pm$ 0.041	45.023 $\pm$ 2.906	24.1	4.210 $\pm$ 0.874	15.0 $\pm$ 3.1
U0800411	19.259 $\pm$ 0.219	0.028 $\pm$ 0.001	0.004 $\pm$ 0.040	51.722 $\pm$ 2.270	20.6	3.976 $\pm$ 0.684	14.2 $\pm$ 2.4
U0800412	21.240 $\pm$ 0.307	0.025 $\pm$ 0.002	0.105 $\pm$ 0.054	56.186 $\pm$ 4.332	21.9	4.651 $\pm$ 1.274	16.6 $\pm$ 4.5
U0800414	32.043 $\pm$ 0.475	0.030 $\pm$ 0.002	0.003 $\pm$ 0.031	86.290 $\pm$ 3.335	20.4	6.544 $\pm$ 1.005	23.3 $\pm$ 3.6
U0800415	44.170 $\pm$ 0.501	0.040 $\pm$ 0.003	0.036 $\pm$ 0.074	135.338 $\pm$ 4.710	9.5	4.183 $\pm$ 1.417	14.9 $\pm$ 5.0
U0800417	37.025 $\pm$ 0.316	0.035 $\pm$ 0.001	0.009 $\pm$ 0.038	107.824 $\pm$ 2.636	13.9	5.164 $\pm$ 0.799	18.4 $\pm$ 2.8
U0800418	21.184 $\pm$ 0.153	0.025 $\pm$ 0.002	0.008 $\pm$ 0.028	57.010 $\pm$ 1.706	20.5	4.339 $\pm$ 0.498	15.5 $\pm$ 1.8
U0800419	17.210 $\pm$ 0.152	0.026 $\pm$ 0.002	0.008 $\pm$ 0.014	41.847 $\pm$ 1.737	28.2	4.845 $\pm$ 0.522	17.3 $\pm$ 1.9
U0800420	21.047 $\pm$ 0.157	0.028 $\pm$ 0.001	0.068 $\pm$ 0.017	53.091 $\pm$ 0.968	25.5	5.368 $\pm$ 0.300	19.1 $\pm$ 1.1
U0800422	105.072 $\pm$ 0.525	0.086 $\pm$ 0.002	0.004 $\pm$ 0.024	340.717 $\pm$ 2.181	4.2	4.391 $\pm$ 0.513	15.6 $\pm$ 1.8
<i>Sample DOT 053A (J = 0.001987)</i>							
U0801401	26.260 $\pm$ 0.390	0.034 $\pm$ 0.003	0.041 $\pm$ 0.036	71.086 $\pm$ 3.815	20.0	5.259 $\pm$ 1.100	18.8 $\pm$ 3.9
U0801402	32.084 $\pm$ 0.302	0.041 $\pm$ 0.004	0.083 $\pm$ 0.045	94.347 $\pm$ 4.177	13.1	4.215 $\pm$ 1.222	15.0 $\pm$ 4.3
U0801403	14.514 $\pm$ 0.104	0.025 $\pm$ 0.002	0.014 $\pm$ 0.014	30.891 $\pm$ 1.411	37.1	5.388 $\pm$ 0.425	19.2 $\pm$ 1.5
U0801404	14.141 $\pm$ 0.502	0.027 $\pm$ 0.001	0.005 $\pm$ 0.005	33.789 $\pm$ 1.178	29.4	4.157 $\pm$ 0.490	14.8 $\pm$ 1.7
U0801405	17.886 $\pm$ 0.133	0.028 $\pm$ 0.001	0.000 $\pm$ 0.006	43.858 $\pm$ 1.192	27.5	4.926 $\pm$ 0.359	17.6 $\pm$ 1.3
U0801406	19.428 $\pm$ 0.129	0.030 $\pm$ 0.001	0.021 $\pm$ 0.006	49.533 $\pm$ 0.864	24.7	4.793 $\pm$ 0.262	17.1 $\pm$ 0.9
U0801407	18.740 $\pm$ 0.138	0.029 $\pm$ 0.001	0.006 $\pm$ 0.009	47.013 $\pm$ 1.102	25.9	4.848 $\pm$ 0.333	17.3 $\pm$ 1.2
U0801408	40.382 $\pm$ 0.201	0.043 $\pm$ 0.001	0.180 $\pm$ 0.021	117.210 $\pm$ 1.672	14.3	5.769 $\pm$ 0.481	20.6 $\pm$ 1.7
U0801409	35.122 $\pm$ 0.118	0.039 $\pm$ 0.001	0.055 $\pm$ 0.012	98.867 $\pm$ 1.227	16.8	5.914 $\pm$ 0.359	21.1 $\pm$ 1.3
U0801410	26.006 $\pm$ 0.099	0.036 $\pm$ 0.001	0.007 $\pm$ 0.007	69.320 $\pm$ 1.197	21.2	5.522 $\pm$ 0.350	19.7 $\pm$ 1.2
U0801411	13.663 $\pm$ 0.160	0.024 $\pm$ 0.001	0.049 $\pm$ 0.008	29.865 $\pm$ 0.674	35.5	4.844 $\pm$ 0.225	17.3 $\pm$ 0.8
U0801412	67.729 $\pm$ 0.229	0.061 $\pm$ 0.001	0.022 $\pm$ 0.005	214.399 $\pm$ 1.222	6.5	4.377 $\pm$ 0.357	15.6 $\pm$ 1.3
U0801413	18.711 $\pm$ 0.112	0.028 $\pm$ 0.001	0.013 $\pm$ 0.015	49.518 $\pm$ 0.780	21.8	4.080 $\pm$ 0.240	14.6 $\pm$ 0.9
U0801414	40.563 $\pm$ 0.191	0.045 $\pm$ 0.001	0.005 $\pm$ 0.008	122.446 $\pm$ 0.998	10.8	4.381 $\pm$ 0.261	15.6 $\pm$ 0.9
<i>Sample GRU 057 (J = 0.001982)</i>							
U0800423	16.203 $\pm$ 0.189	0.025 $\pm$ 0.003	4.031 $\pm$ 0.112	46.681 $\pm$ 4.403	18.0	2.922 $\pm$ 1.314	10.4 $\pm$ 4.7
U0800501	19.220 $\pm$ 0.193	0.027 $\pm$ 0.004	0.807 $\pm$ 0.099	55.037 $\pm$ 5.047	15.9	3.059 $\pm$ 1.497	10.9 $\pm$ 5.3
U0800506	14.118 $\pm$ 0.104	0.027 $\pm$ 0.003	0.413 $\pm$ 0.048	31.101 $\pm$ 2.117	35.3	4.981 $\pm$ 0.629	17.7 $\pm$ 2.2
U0800509	59.368 $\pm$ 0.923	0.048 $\pm$ 0.004	0.512 $\pm$ 0.077	183.229 $\pm$ 5.137	8.9	5.290 $\pm$ 1.308	18.8 $\pm$ 4.6
U0800512	32.720 $\pm$ 0.358	0.033 $\pm$ 0.003	0.713 $\pm$ 0.079	95.548 $\pm$ 3.578	14.0	4.577 $\pm$ 1.051	16.3 $\pm$ 3.7
U0800514	36.416 $\pm$ 0.388	0.032 $\pm$ 0.002	0.302 $\pm$ 0.058	108.078 $\pm$ 2.784	12.4	4.518 $\pm$ 0.807	16.1 $\pm$ 2.9
U0800516	47.245 $\pm$ 0.540	0.052 $\pm$ 0.006	5.407 $\pm$ 0.153	146.988 $\pm$ 5.069	9.5	4.507 $\pm$ 1.449	16.0 $\pm$ 5.1
U0800518	21.730 $\pm$ 0.154	0.024 $\pm$ 0.003	1.974 $\pm$ 0.134	57.416 $\pm$ 3.090	23.1	5.019 $\pm$ 0.918	17.9 $\pm$ 3.3
U0800519	27.970 $\pm$ 0.297	0.029 $\pm$ 0.004	2.521 $\pm$ 0.162	80.772 $\pm$ 4.350	15.8	4.427 $\pm$ 1.297	15.8 $\pm$ 4.6
U0800520	26.896 $\pm$ 0.505	0.033 $\pm$ 0.006	5.691 $\pm$ 0.337	76.632 $\pm$ 6.459	18.4	4.987 $\pm$ 1.923	17.7 $\pm$ 6.8
U0800521	16.096 $\pm$ 0.271	0.022 $\pm$ 0.003	0.469 $\pm$ 0.076	43.933 $\pm$ 2.590	19.7	3.174 $\pm$ 0.776	11.3 $\pm$ 2.8
U0800522	27.070 $\pm$ 0.288	0.024 $\pm$ 0.002	1.497 $\pm$ 0.081	77.285 $\pm$ 4.495	16.3	4.426 $\pm$ 1.335	15.8 $\pm$ 4.7
U0800526	28.451 $\pm$ 0.543	0.041 $\pm$ 0.004	3.301 $\pm$ 0.123	79.388 $\pm$ 3.095	19.0	5.420 $\pm$ 0.854	19.3 $\pm$ 3.0
U0800527	22.738 $\pm$ 0.378	0.031 $\pm$ 0.006	3.287 $\pm$ 0.114	61.476 $\pm$ 3.441	21.9	4.997 $\pm$ 1.055	17.8 $\pm$ 3.7
U0800530	49.798 $\pm$ 0.662	0.045 $\pm$ 0.002	1.052 $\pm$ 0.054	151.435 $\pm$ 4.707	10.4	5.185 $\pm$ 1.274	18.4 $\pm$ 4.5
U0801111	67.431 $\pm$ 0.511	0.057 $\pm$ 0.004	2.689 $\pm$ 0.161	217.685 $\pm$ 6.163	5.1	3.449 $\pm$ 1.792	12.3 $\pm$ 6.4
U0801112	32.932 $\pm$ 0.330	0.038 $\pm$ 0.006	2.216 $\pm$ 0.242	98.579 $\pm$ 5.533	12.4	4.086 $\pm$ 1.654	14.6 $\pm$ 5.9
<i>Sample MOL 055 (J = 0.001980)</i>							
U0801302	11.432 $\pm$ 0.214	0.026 $\pm$ 0.002	0.030 $\pm$ 0.058	19.178 $\pm$ 3.209	50.5	5.769 $\pm$ 0.958	20.5 $\pm$ 3.4
U0801303	25.711 $\pm$ 0.352	0.027 $\pm$ 0.003	0.038 $\pm$ 0.056	70.910 $\pm$ 3.824	18.5	4.762 $\pm$ 1.126	16.9 $\pm$ 4.0
U0801304	16.672 $\pm$ 0.249	0.026 $\pm$ 0.002	0.088 $\pm$ 0.040	38.893 $\pm$ 3.999	31.1	5.190 $\pm$ 1.197	18.4 $\pm$ 4.2
U0801305	16.077 $\pm$ 0.303	0.025 $\pm$ 0.003	0.247 $\pm$ 0.082	38.409 $\pm$ 5.093	29.6	4.759 $\pm$ 1.512	16.9 $\pm$ 5.4
U0801306	16.248 $\pm$ 0.367	0.027 $\pm$ 0.003	0.266 $\pm$ 0.090	33.941 $\pm$ 7.792	38.5	6.253 $\pm$ 2.317	22.2 $\pm$ 8.2
U0801307	22.191 $\pm$ 0.588	0.031 $\pm$ 0.006	0.057 $\pm$ 0.116	55.736 $\pm$ 8.440	25.8	5.729 $\pm$ 2.513	20.3 $\pm$ 8.9
U0801308	17.161 $\pm$ 0.432	0.031 $\pm$ 0.005	0.399 $\pm$ 0.097	41.457 $\pm$ 9.153	28.9	4.962 $\pm$ 2.723	17.6 $\pm$ 9.6
U0801309	21.317 $\pm$ 0.383	0.032 $\pm$ 0.004	0.069 $\pm$ 0.171	58.324 $\pm$ 5.714	19.2	4.091 $\pm$ 1.713	14.6 $\pm$ 6.1
U0801310	14.616 $\pm$ 0.329	0.017 $\pm$ 0.004	0.058 $\pm$ 0.186	33.662 $\pm$ 5.053	32.0	4.676 $\pm$ 1.507	16.6 $\pm$ 5.3
U0801311	10.646 $\pm$ 0.144	0.022 $\pm$ 0.002	0.168 $\pm$ 0.105	18.222 $\pm$ 3.140	49.6	5.283 $\pm$ 0.934	18.8 $\pm$ 3.3

<sup>a</sup>Uncertainties are given in  $1\sigma$ ; error on single ages does not include the uncertainty in the J value.

yield a weighted average age of  $18.36 \pm 1.52$  Ma (Figure 7d). This is only slightly older compared to the weighted average ages of the other three samples studied.

### 5.3. The $^{40}\text{Ar}/^{39}\text{Ar}$ CO<sub>2</sub> Laser Stepwise Heating of Biotite

[39] The  $^{40}\text{Ar}/^{39}\text{Ar}$  age spectra for biotite separated from five samples show rather simple and well-developed plateaus

**Table 4.** Full Results of  $^{40}\text{Ar}/^{39}\text{Ar}$  CO<sub>2</sub> Laser Stepwise Heating Analysis of Biotite<sup>a</sup>

Step	Laser Output	$^{40}\text{Ar}/^{39}\text{Ar}$	$^{38}\text{Ar}/^{39}\text{Ar}$	$^{37}\text{Ar}/^{39}\text{Ar}$	$^{36}\text{Ar}/^{39}\text{Ar}$ ( $\times 10^{-3}$ )	$^{40}\text{Ar}^*$ (%)	$^{39}\text{Ar}_K$ (%)	$^{40}\text{Ar}^*/^{39}\text{Ar}_K$	Age (Ma) $\pm 1\sigma$
<i>Sample LUZ 0444 (J = 0.001968)</i>									
1	1.2	17675.104 $\pm$ 909.449	12.0537 $\pm$ 0.6429	0.983 $\pm$ 1.475	60562.730 $\pm$ 3124.476	0.0	0.1	0.105 $\pm$ 71.473	0.4 $\pm$ 253.7
2	1.4	3256.322 $\pm$ 54.969	2.1516 $\pm$ 0.0403	0.259 $\pm$ 0.139	11206.461 $\pm$ 190.564	-1.7	0.4	-55.168 $\pm$ -8.161	-207.3 $\pm$ -32.5
3	1.6	403.998 $\pm$ 2.312	0.2765 $\pm$ 0.0049	0.017 $\pm$ 0.025	1375.101 $\pm$ 10.992	-0.6	1.7	-2.342 $\pm$ -2.371	-8.3 $\pm$ -8.5
4	1.8	102.561 $\pm$ 0.321	0.0855 $\pm$ 0.0007	0.003 $\pm$ 0.004	341.074 $\pm$ 1.668	1.7	11.2	1.774 $\pm$ 0.477	6.3 $\pm$ 1.7
5	2.0	26.702 $\pm$ 0.088	0.0327 $\pm$ 0.0003	0.001 $\pm$ 0.002	75.297 $\pm$ 0.358	16.7	25.7	4.451 $\pm$ 0.106	15.7 $\pm$ 0.4
6	2.2	10.835 $\pm$ 0.025	0.0231 $\pm$ 0.0001	0.005 $\pm$ 0.001	20.072 $\pm$ 0.121	45.3	22.7	4.904 $\pm$ 0.039	17.3 $\pm$ 0.2
7	2.4	9.190 $\pm$ 0.030	0.0221 $\pm$ 0.0001	0.011 $\pm$ 0.002	14.373 $\pm$ 0.075	53.8	10.8	4.944 $\pm$ 0.030	17.5 $\pm$ 0.1
8	2.8	7.720 $\pm$ 0.022	0.0213 $\pm$ 0.0001	0.016 $\pm$ 0.009	9.212 $\pm$ 0.089	64.8	14.7	5.000 $\pm$ 0.031	17.7 $\pm$ 0.1
9	3.2	6.764 $\pm$ 0.015	0.0216 $\pm$ 0.0002	0.024 $\pm$ 0.026	6.658 $\pm$ 0.069	71.0	9.2	4.799 $\pm$ 0.024	17.0 $\pm$ 0.1
10	3.6	6.097 $\pm$ 0.041	0.0203 $\pm$ 0.0003	0.046 $\pm$ 0.007	4.614 $\pm$ 0.151	77.7	2.5	4.739 $\pm$ 0.057	16.7 $\pm$ 0.2
11	4.0-4.4	6.752 $\pm$ 0.074	0.0214 $\pm$ 0.0011	0.361 $\pm$ 0.156	8.653 $\pm$ 0.463	62.8	0.6	4.241 $\pm$ 0.150	15.0 $\pm$ 0.5
12	4.8-5.2	11.831 $\pm$ 0.345	0.0289 $\pm$ 0.0041	0.678 $\pm$ 1.138	32.440 $\pm$ 4.791	19.7	0.1	2.331 $\pm$ 1.445	8.3 $\pm$ 5.1
13	6.0	10.793 $\pm$ 0.235	0.0317 $\pm$ 0.0023	1.049 $\pm$ 0.199	23.532 $\pm$ 2.013	36.8	0.2	3.974 $\pm$ 0.612	14.1 $\pm$ 2.2
<i>Sample BLE 0513 (J = 0.001976)</i>									
1	1.2	43727.734 $\pm$ 526.768	29.2058 $\pm$ 0.4093	1.500 $\pm$ 1.104	154713.189 $\pm$ 1866.944	0.0	0.0	0.270 $\pm$ 55.363	1.0 $\pm$ 197.3
2	1.4	7165.997 $\pm$ 68.998	4.7195 $\pm$ 0.0635	0.270 $\pm$ 0.198	24835.872 $\pm$ 241.040	-2.4	0.3	-173.011 $\pm$ -9.624	-754.7 $\pm$ -52.3
3	1.6	423.712 $\pm$ 2.601	0.2830 $\pm$ 0.0038	0.050 $\pm$ 0.037	1441.461 $\pm$ 9.752	-0.5	1.4	-2.234 $\pm$ -1.263	-8.0 $\pm$ -4.5
4	1.8	97.399 $\pm$ 0.185	0.0760 $\pm$ 0.0006	0.039 $\pm$ 0.041	314.990 $\pm$ 0.949	4.4	6.5	4.325 $\pm$ 0.241	15.4 $\pm$ 0.9
5	2.0	35.691 $\pm$ 0.063	0.0388 $\pm$ 0.0002	0.009 $\pm$ 0.001	109.182 $\pm$ 0.330	9.6	14.3	3.429 $\pm$ 0.097	12.2 $\pm$ 0.3
6	2.2	20.221 $\pm$ 0.057	0.0290 $\pm$ 0.0002	0.010 $\pm$ 0.001	55.018 $\pm$ 0.200	19.6	13.3	3.964 $\pm$ 0.061	14.1 $\pm$ 0.2
7	2.4	14.856 $\pm$ 0.048	0.0250 $\pm$ 0.0002	0.012 $\pm$ 0.002	35.784 $\pm$ 0.223	28.8	10.8	4.284 $\pm$ 0.070	15.2 $\pm$ 0.3
8	2.6	11.009 $\pm$ 0.021	0.0230 $\pm$ 0.0002	0.011 $\pm$ 0.002	22.479 $\pm$ 0.097	39.7	11.8	4.367 $\pm$ 0.030	15.5 $\pm$ 0.1
9	2.8	10.898 $\pm$ 0.031	0.0225 $\pm$ 0.0001	0.011 $\pm$ 0.002	22.248 $\pm$ 0.135	39.7	11.5	4.326 $\pm$ 0.045	15.4 $\pm$ 0.2
10	3.0	12.526 $\pm$ 0.035	0.0239 $\pm$ 0.0002	0.012 $\pm$ 0.002	27.860 $\pm$ 0.163	34.3	10.8	4.295 $\pm$ 0.051	15.2 $\pm$ 0.2
11	3.2	10.527 $\pm$ 0.041	0.0221 $\pm$ 0.0001	0.016 $\pm$ 0.002	20.211 $\pm$ 0.190	43.3	8.2	4.557 $\pm$ 0.061	16.2 $\pm$ 0.2
12	3.4	8.751 $\pm$ 0.055	0.0223 $\pm$ 0.0004	0.027 $\pm$ 0.004	15.008 $\pm$ 0.265	49.4	4.9	4.320 $\pm$ 0.087	15.3 $\pm$ 0.3
13	3.8	7.444 $\pm$ 0.056	0.0192 $\pm$ 0.0003	0.027 $\pm$ 0.005	10.363 $\pm$ 0.161	58.9	4.8	4.385 $\pm$ 0.064	15.6 $\pm$ 0.2
14	4.2-5.0	7.399 $\pm$ 0.099	0.0190 $\pm$ 0.0009	0.115 $\pm$ 0.021	8.144 $\pm$ 0.543	67.7	1.1	5.008 $\pm$ 0.182	17.8 $\pm$ 0.6
15	5.4	9.975 $\pm$ 0.202	0.0226 $\pm$ 0.0017	0.467 $\pm$ 0.346	13.651 $\pm$ 2.634	60.1	0.3	6.002 $\pm$ 0.796	21.3 $\pm$ 2.8
<i>Sample DOT 053A (J = 0.001963)</i>									
1	1.2	25033.052 $\pm$ 488.166	16.7006 $\pm$ 0.3593	0.774 $\pm$ 1.523	87645.099 $\pm$ 1706.561	0.0	0.1	0.207 $\pm$ 42.711	0.7 $\pm$ 151.2
2	1.4	4280.595 $\pm$ 32.157	2.8717 $\pm$ 0.0291	0.252 $\pm$ 0.361	14889.006 $\pm$ 120.536	-2.8	0.3	-119.101 $\pm$ -14.967	-480.4 $\pm$ -69.2
3	1.6	198.456 $\pm$ 0.860	0.1501 $\pm$ 0.0012	0.094 $\pm$ 0.013	677.009 $\pm$ 2.838	-0.8	3.1	-1.588 $\pm$ -0.428	-5.6 $\pm$ -1.5
4	1.8	45.448 $\pm$ 0.122	0.0465 $\pm$ 0.0004	0.004 $\pm$ 0.007	141.421 $\pm$ 0.529	8.0	11.0	3.658 $\pm$ 0.154	12.9 $\pm$ 0.5
5	2.0	23.383 $\pm$ 0.069	0.0334 $\pm$ 0.0003	0.045 $\pm$ 0.047	64.635 $\pm$ 0.324	18.3	13.6	4.289 $\pm$ 0.097	15.1 $\pm$ 0.3
6	2.2	14.572 $\pm$ 0.041	0.0281 $\pm$ 0.0002	0.001 $\pm$ 0.004	34.111 $\pm$ 0.126	30.8	11.6	4.493 $\pm$ 0.040	15.8 $\pm$ 0.2
7	2.4	10.752 $\pm$ 0.028	0.0256 $\pm$ 0.0004	0.019 $\pm$ 0.021	20.864 $\pm$ 0.183	42.7	11.9	4.589 $\pm$ 0.055	16.2 $\pm$ 0.2
8	2.8	9.293 $\pm$ 0.025	0.0248 $\pm$ 0.0002	0.163 $\pm$ 0.023	15.476 $\pm$ 0.125	51.0	25.5	4.740 $\pm$ 0.041	16.7 $\pm$ 0.2
9	3.2	7.763 $\pm$ 0.021	0.0231 $\pm$ 0.0001	0.056 $\pm$ 0.033	10.303 $\pm$ 0.116	60.9	17.7	4.726 $\pm$ 0.038	16.7 $\pm$ 0.1
10	3.6	7.265 $\pm$ 0.028	0.0232 $\pm$ 0.0004	0.199 $\pm$ 0.054	9.138 $\pm$ 0.154	63.2	4.4	4.590 $\pm$ 0.051	16.2 $\pm$ 0.2
11	4.0	7.145 $\pm$ 0.205	0.0274 $\pm$ 0.0022	1.160 $\pm$ 0.836	12.312 $\pm$ 2.917	51.1	0.2	3.655 $\pm$ 0.889	12.9 $\pm$ 3.1
12	6.0	9.022 $\pm$ 0.217	0.0219 $\pm$ 0.0019	1.844 $\pm$ 0.788	16.061 $\pm$ 1.337	49.9	0.5	4.514 $\pm$ 0.440	15.9 $\pm$ 1.5
<i>Sample GRU 062 (J = 0.001959)</i>									
1	1.2	56609.150 $\pm$ 6045.036	37.7322 $\pm$ 4.0417	6.488 $\pm$ 7.078	193499.384 $\pm$ 20677.217	0.0	0.0	0.288 $\pm$ 233.779	1.0 $\pm$ 825.8
2	1.4	10959.587 $\pm$ 235.825	7.2126 $\pm$ 0.1899	0.928 $\pm$ 1.488	37003.926 $\pm$ 810.389	0.2	0.2	25.063 $\pm$ 45.101	86.5 $\pm$ 151.9
3	1.6	795.761 $\pm$ 2.112	0.5316 $\pm$ 0.0107	0.285 $\pm$ 0.282	2717.895 $\pm$ 10.679	-0.9	0.8	-7.343 $\pm$ -2.617	-26.1 $\pm$ -9.4
4	1.8	132.505 $\pm$ 0.384	0.1002 $\pm$ 0.0017	0.010 $\pm$ 0.018	444.773 $\pm$ 1.722	0.8	4.9	1.076 $\pm$ 0.456	3.8 $\pm$ 1.6
5	2.0	36.626 $\pm$ 0.110	0.0388 $\pm$ 0.0003	0.003 $\pm$ 0.006	107.980 $\pm$ 0.378	12.9	14.8	4.718 $\pm$ 0.108	16.6 $\pm$ 0.4
6	2.2	20.435 $\pm$ 0.039	0.0277 $\pm$ 0.0002	0.012 $\pm$ 0.003	54.407 $\pm$ 0.182	21.3	18.9	4.359 $\pm$ 0.056	15.3 $\pm$ 0.2
7	2.4	15.940 $\pm$ 0.047	0.0243 $\pm$ 0.0002	0.044 $\pm$ 0.022	39.138 $\pm$ 0.186	27.5	15.3	4.380 $\pm$ 0.058	15.4 $\pm$ 0.2
8	2.6	12.626 $\pm$ 0.033	0.0222 $\pm$ 0.0003	0.035 $\pm$ 0.036	27.573 $\pm$ 0.256	35.5	8.5	4.482 $\pm$ 0.078	15.8 $\pm$ 0.3
9	3.0	13.100 $\pm$ 0.031	0.0223 $\pm$ 0.0002	0.004 $\pm$ 0.005	29.230 $\pm$ 0.125	34.1	15.2	4.463 $\pm$ 0.038	15.7 $\pm$ 0.1
10	3.4	14.086 $\pm$ 0.038	0.0230 $\pm$ 0.0002	0.031 $\pm$ 0.014	32.810 $\pm$ 0.150	31.2	12.5	4.394 $\pm$ 0.047	15.5 $\pm$ 0.2
11	3.8	13.494 $\pm$ 0.042	0.0228 $\pm$ 0.0003	0.027 $\pm$ 0.031	30.561 $\pm$ 0.303	33.1	5.9	4.466 $\pm$ 0.089	15.7 $\pm$ 0.3
12	4.4-5.0	12.684 $\pm$ 0.038	0.0220 $\pm$ 0.0004	0.167 $\pm$ 0.134	28.488 $\pm$ 0.448	33.8	2.6	4.288 $\pm$ 0.135	15.1 $\pm$ 0.5
13	5.6-7.0	16.351 $\pm$ 0.264	0.0258 $\pm$ 0.0033	1.136 $\pm$ 0.797	31.134 $\pm$ 2.423	44.6	0.2	7.300 $\pm$ 0.728	25.6 $\pm$ 2.5
<i>Sample MOL 054 (J = 0.001954)</i>									
1	1.2	16964.056 $\pm$ 1316.759	11.1312 $\pm$ 0.8710	0.870 $\pm$ 0.699	58425.668 $\pm$ 4536.218	0.0	0.1	0.158 $\pm$ 34.703	0.6 $\pm$ 122.3
2	1.4	1612.333 $\pm$ 7.062	1.0799 $\pm$ 0.0091	0.175 $\pm$ 0.126	5454.611 $\pm$ 24.724	0.0	0.6	0.517 $\pm$ 2.184	1.8 $\pm$ 7.7
3	1.6	132.049 $\pm$ 0.254	0.1051 $\pm$ 0.0008	0.021 $\pm$ 0.009	441.656 $\pm$ 1.213	1.2	5.1	1.542 $\pm$ 0.266	5.4 $\pm$ 0.9
4	1.8	32.272 $\pm$ 0.049	0.0390 $\pm$ 0.0002	0.007 $\pm$ 0.003	96.044 $\pm$ 0.330	12.1	16.5	3.891 $\pm$ 0.090	13.7 $\pm$ 0.3
5	2.0	12.861 $\pm$ 0.019	0.0264 $\pm$ 0.0002	0.005 $\pm$ 0.009	28.535 $\pm$ 0.131	34.4	19.7	4.429 $\pm$ 0.040	15.5 $\pm$ 0.2

**Table 4.** (continued)

Laser Step	Output	$^{40}\text{Ar}/^{39}\text{Ar}$	$^{38}\text{Ar}/^{39}\text{Ar}$	$^{37}\text{Ar}/^{39}\text{Ar}$	$^{36}\text{Ar}/^{39}\text{Ar}$ ( $\times 10^{-3}$ )	$^{40}\text{Ar}^*$ (%)	$^{39}\text{Ar}_K$ (%)	$^{40}\text{Ar}^*/^{39}\text{Ar}_K$	Age (Ma) $\pm 1\sigma$
6	2.2	$9.633 \pm 0.040$	$0.0234 \pm 0.0002$	$0.008 \pm 0.001$	$16.771 \pm 0.151$	48.6	13.8	$4.678 \pm 0.052$	$16.4 \pm 0.2$
7	2.4	$9.508 \pm 0.046$	$0.0235 \pm 0.0002$	$0.010 \pm 0.001$	$16.520 \pm 0.168$	48.7	10.7	$4.628 \pm 0.057$	$16.2 \pm 0.2$
8	2.8	$11.545 \pm 0.026$	$0.0260 \pm 0.0003$	$0.006 \pm 0.001$	$23.586 \pm 0.087$	39.6	17.6	$4.576 \pm 0.029$	$16.1 \pm 0.1$
9	3.2	$9.310 \pm 0.046$	$0.0243 \pm 0.0004$	$0.017 \pm 0.016$	$16.146 \pm 0.226$	48.8	10.5	$4.541 \pm 0.073$	$15.9 \pm 0.3$
10	3.6	$8.568 \pm 0.062$	$0.0253 \pm 0.0005$	$0.027 \pm 0.028$	$12.155 \pm 0.308$	58.1	3.0	$4.980 \pm 0.104$	$17.5 \pm 0.4$
11	4.0–4.8	$10.972 \pm 0.088$	$0.0234 \pm 0.0007$	$0.022 \pm 0.028$	$17.978 \pm 0.316$	51.6	2.3	$5.663 \pm 0.112$	$19.9 \pm 0.4$

<sup>a</sup>Uncertainties are given in  $1\sigma$ ; error on single ages does not include the uncertainty in the J value. The  $^{39}\text{Ar}_K$  is the percentile fraction of K-derived  $^{39}\text{Ar}$ .

that yield consistent ages between 17.27 and 15.48 Ma (Figure 8 and Table 4). Generally a significant plateau age is defined by (1) the occurrence of a series of adjacent steps that together comprise more than 50% of the total  $^{39}\text{Ar}$  release, (2) the ages agree within  $2\sigma$  error limits (excluding uncertainties in the J value) between each contiguous two fractions, and (3) one fraction consisting of the plateau comprises more than 3% of the total  $^{39}\text{Ar}$  release [see *McDougall and Harrison*, 1999, and references therein]; being aware that there is still a wide debate if a plateau age ever has any significance [e.g., *Hodges et al.*, 1994]. However, the plateaus recorded in this study satisfy these conditions. The average grain size for all biotite separates was in the same range and varied between 250 and 315  $\mu\text{m}$ . Usually, the first

five or six low temperature steps, and in a less pronounced manner the last steps at high temperatures, are characterized by a disturbed pattern. Hence, the total gas ages, calculated by integrating over all steps, have no geological significance; they are between 3.04 and 0.6 Ma younger compared to the plateau ages (Figure 8).

## 6. Interpretations and Discussion

### 6.1. Interpretation of Individual Age Data

[40] In general the presence of extraneous  $^{40}\text{Ar}$  (excess or inherited argon) is due to the incorporation of additional  $^{40}\text{Ar}$  by processes other than in situ decay. It may be of external origin by diffusion through grain boundaries (excess argon)

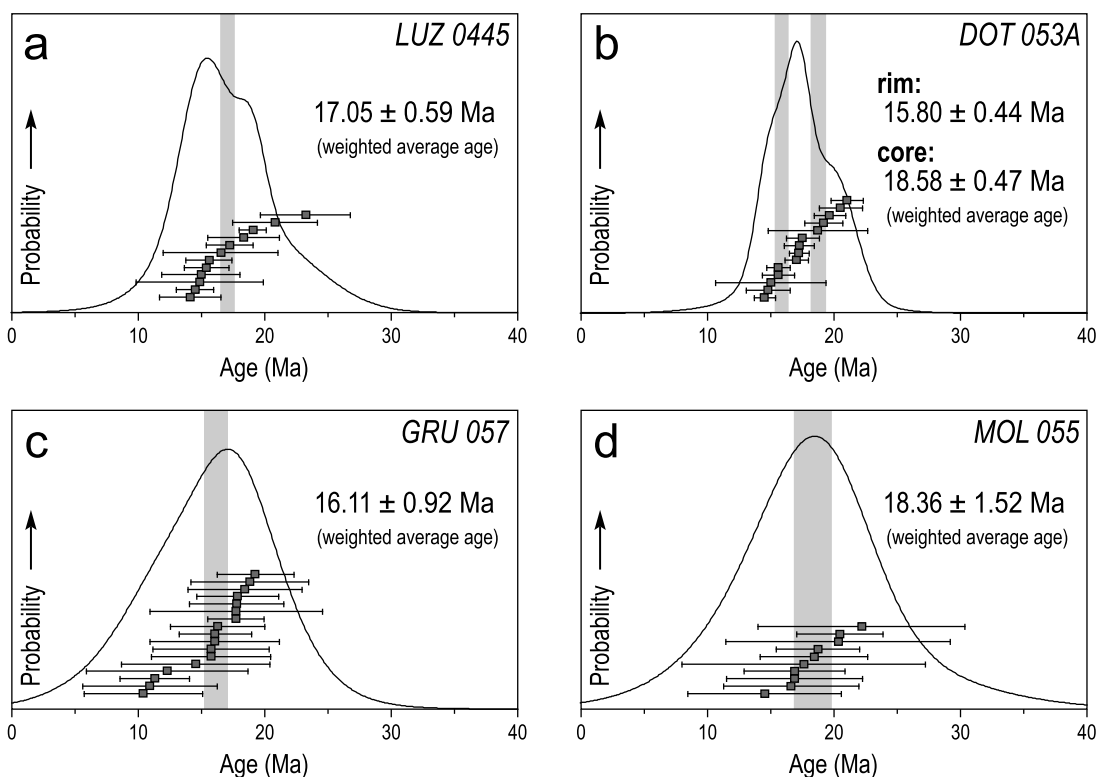


**Figure 7.** Summary of apparent ages obtained on biotite by in situ laser probe analyses and calculated cumulative probability curves. The resulting weighted average age is also denoted; errors are  $1\sigma$  and do not include the uncertainty in the J value. (a) Sample LUZ 0445. (b) Sample DOT 053A. (c) Sample GRU 057. (d) Sample MOL 055.

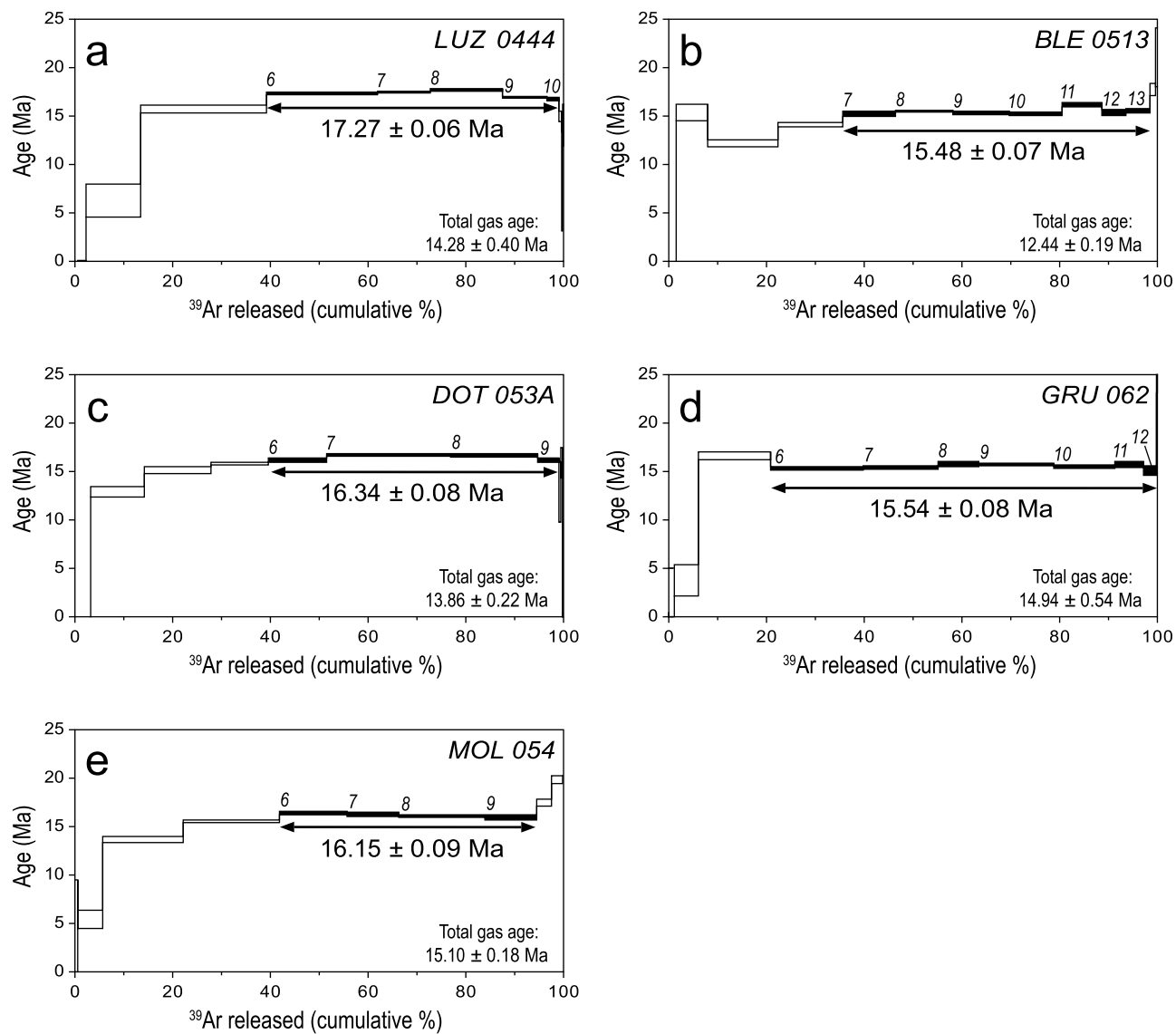


**Figure 8.** Biotite  $^{40}\text{Ar}/^{39}\text{Ar}$  age spectra obtained by stepwise heating experiments. Total gas ages were determined by integrating over all steps. Steps attributed to the plateau are highlighted in black. Numbers refer to steps used for the calculation of the plateau ages. Uncertainties are given in  $1\sigma$  and do not include the uncertainty in the  $J$  value. (a) Sample LUZ 0444. (b) Sample BLE 0513. (c) Sample DOT 053A. (d) Sample GRU 062. (e) Sample MOL 054.

or, alternatively by the presence of inherited argon in an incompletely rejuvenated metamorphic mineral [Lanphere and Dalrymple, 1976]. In any case ages affected by the presence of extraneous  $^{40}\text{Ar}$  yield consequently older ages with absolutely no geological significance. Several studies have shown that extraneous argon is commonly found in high-pressure and ultrahigh-pressure metamorphic rocks [e.g., Scaillet, 1996; Sherlock and Kelley, 2002; Di Vincenzo *et al.*, 2006, and references therein]. However, in our samples we find no indications for excess Ar. As shown later on, also the internal consistency of the data with microstructural data and structural field data, and additionally, the overlap with published results using independent methods (e.g., U-Th-Pb

in allanite and monazite by Janots *et al.* [2009]) confirm the absence of excess Ar problems in the case of our samples.

[41] K/Ar (and Ar/Ar) data were often interpreted in the context of the “blocking temperature” [Jäger *et al.*, 1967] or “closure temperature” [Dodson, 1973] concept. The pioneering study of Purdy and Jäger [1976] proposed a “closure temperature” of  $350^\circ\text{C}$  for the K-Ar isotopic system in muscovite. More modern studies increased this value up to some  $550^\circ\text{C}$  or even more [Di Vincenzo *et al.*, 2001; Philippot *et al.*, 2001; Bucher, 2003; Balogh and Dunkl, 2005; Allaz, 2008]. On the other hand it has been shown that metamorphic reactions and/or deformation, commonly enhanced by the presence of a fluid, may induce isotopic

resetting [e.g., *Foland*, 1979; *Chopin and Maluski*, 1980; *Chopin and Monié*, 1984; *Wijbrans and McDougall*, 1986; *Villa*, 1998; *Bucher*, 2003; *Di Vincenzo et al.*, 2004; *Gouzu et al.*, 2006; *Glodny et al.*, 2008a, 2008b]. In case of the phengites investigated by this study peak metamorphic temperatures of around ca. 350°C are estimated for the occurrences in the Engadine window [*Bousquet et al.*, 1998] and some 350–400°C for those from Safiental and Valsertal [*Bousquet et al.*, 2002; *Wiederkehr*, 2009]. Hence, the peak metamorphic temperatures of all studied phengite are just at or below the range of suggested “closure temperatures.” Moreover, there is microstructural evidence for retrograde metamorphic reactions that are associated with recrystallization. In summary, we interpret the recorded apparent ages of the studied phengites as formation/crystallization ages. We explain the observed scatter in age by the existence of mixed populations. This implies that even high-pressure relics can survive subsequent deformation and metamorphism, in accordance with recent observations [e.g., *Agard et al.*, 2002; *Bucher*, 2003; *Villa*, 2006].

[42] Biotite bearing samples reached significantly higher peak metamorphic temperatures ranging from 475 to 525°C near the biotite-in isograd in Val Luzzzone to 560–590°C around Pizzo Molare inside the Lepontine dome (Figure 1b) [*Wiederkehr*, 2009]. Our weighted average ages determined by in situ investigations as well as the recorded plateau ages of biotite (18.36–15.48 Ma, Figures 7 and 8) are slightly younger compared to the thermal peak at 18–19 Ma as presumably dated by U-Pb investigations on monazite [*Janots et al.*, 2009]. This small difference in age is best explained by retrograde chloritization of biotite, as is clearly evidenced by the omnipresence of retrograde chlorite. Hence, the individual apparent ages obtained for biotite are interpreted as formation ages that were rejuvenated by partial reequilibration and major element and isotopic resetting. The interpretation of the isotopic data as (re)crystallization ages instead of cooling ages is supported by the observation that the K-Ar system of biotite may persist through long periods of high temperatures near 600°C and higher as long as the rock remains dry and does not react [*Camacho et al.*, 2005; *Glodny et al.*, 2008b]. In summary, our isotopic data on biotite may be regarded as recrystallization ages that lay somewhere between biotite formation and subsequent retrogression (chloritization), the scatter in the individual ages being due to a variable intensity of chemical reequilibration [*Villa*, 2006; *Allaz*, 2008].

## 6.2. Correlation Between Isotopic Data and Microstructural Features

[43] Recorded apparent ages often correlate with different white mica generations as evidenced by microstructural observations. In our case, the interpretation of apparent ages determined by the in situ laser probe dating technique is unfortunately hampered by the large uncertainties in apparent age, often exceeding 10% for 1 $\sigma$  errors. These large uncertainties are due to the low amount of gas ablated during the laser experiments, caused by the small diameter of the laser spot chosen in order to avoid contaminations by surrounding mineral grains, particularly quartz and chlorite. Overlap

between apparent ages with associated uncertainties precludes the accurate discrimination between different generations based on statistical principles (Figure 9).

[44] Nevertheless, the resulting probability curve can be decomposed into three distinct peaks related to specific age populations in a qualitative way (Figure 9). The main peak at 35–30 Ma is surrounded by a relatively broad shoulder toward older apparent ages, i.e., somewhere between 45 and 40 Ma, and a narrow and well-defined peak that produces a shoulder toward younger ages and located at around 25 Ma. A closer look at the main peak at 35–30 Ma reveals its weakly asymmetric shape with a shoulder toward younger ages. The latter feature possibly suggests that the 35–30 Ma population may consist of two subpopulations; a younger one being located at 30 Ma and an older one at around 35–33 Ma (indicated as gray bars in Figure 9). Sample VAL 0580 yields the youngest and best defined apparent white mica ages, with a weighted average age of 25.40  $\pm$  0.45 (depicted by gray bar in Figure 9), an age that may indeed be responsible for the shoulder visible at around 25 Ma in the probability curve (Figure 9). Such an interpretation is also consistent with the chemical and microstructural data presented above.

[45] The isolated phengite flakes entrapped in quartz invariably yield the oldest individual apparent ages. These are in a range between 44 and 37 Ma (e.g., sample AlpTea 638A; Figures 4b, 4d, and 4e). Numerous fibers of Fe-Mg carpholite are found as inclusions within the same surrounding quartz grain, close to the isolated phengite. Since quartz did not recrystallize into subgrains, clearly the isolated phengite flakes and the relics of carpholite must have been entrapped within quartz under the same metamorphic conditions, i.e., at peak HP/LT conditions. Consequently, we interpret these oldest apparent ages obtained from isolated white mica as dating the peak pressure. Similarly old ages in the range of 45–40 Ma are also found in needle-shaped aggregates (pseudomorphs after carpholite) that consist of white mica, which is intimately associated with chlorite (Figures 4b, 4d, 4h, and 5b). Note also that ages in the range of 45–40 Ma are only found in samples AlpTea 638A, FOT 937, and SAF 0527, i.e., samples characterized the occurrences of white mica showing a considerable celadonite content typical for high-pressure phengite (Figure 3a) [see also *Bousquet et al.*, 1998]. By considering all these ages as representing a single apparent age population a weighted average age of 41.23  $\pm$  1.22 Ma can be calculated as displayed by the gray bar shown in Figure 9. The weighted average age clearly overlaps with the “oldest,” decomposed peak representing the relatively broad shoulder toward older apparent ages of the resulting probability curve, i.e., between 45 and 40 Ma (Figure 9).

[46] Most of the individual apparent ages cluster in the time interval between 36 and 29 Ma as is also indicated by the peak of the probability curve (Figure 9). However, such ages are exclusively found as needle-shaped aggregates that consist of phengite and chlorite and that replace carpholite embedded in quartz, i.e., within pseudomorphs after carpholite. Hence, the associated white mica is unambiguously related to the decay of carpholite, which is in turn induced by substantial decompression along the retrograde path. As

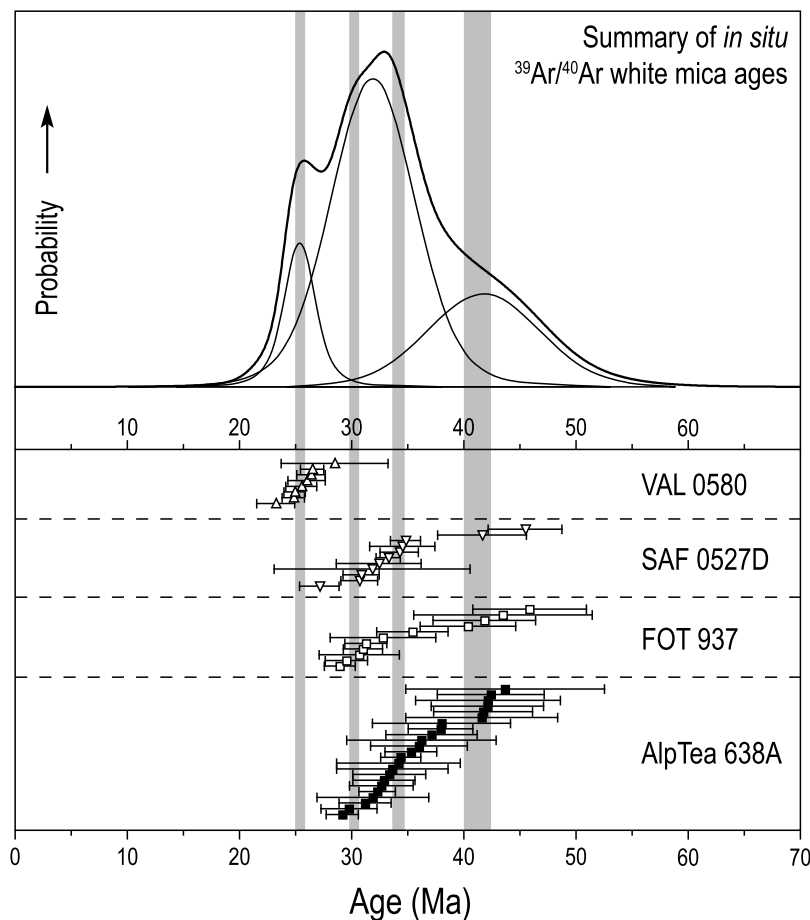


**Figure 9.** Summary of apparent ages obtained on white mica by in situ laser probe analyses and calculated cumulative probability curve. The complex shape of the cumulative probability curve reflects the presence of more than one white mica population as indicated by the decomposition of at least three distinct peaks related to different ages; the light gray bars denote the weighted average ages of the four different populations (see text for discussion). Uncertainties are given in  $1\sigma$  and do not include the uncertainty in the  $J$  value.

mentioned above when discussing the decomposition of the probability curve shown in Figure 9, it is unclear if the range between 36 and 29 Ma represents a single event, or alternatively, a bimodal population. The slightly asymmetric shape of the maximum peak in the probability curve hints toward two distinctive age populations (indicated by the gray bars). Obviously white mica-chlorite aggregates replacing carpholite yield well-defined and accurate apparent ages between 32 and 29 Ma (Figures 4c and 5g), clustering at the lower end of the 36–29 Ma age interval commonly recorded inside such pseudomorphs after carpholite.

[47] In any case, the existence of substantially older ages, i.e., ages between 36 and 34 Ma points to either mixed ages of the older HP/LT event or yet another age population at around 36–34 Ma. Consequently, if the well-defined apparent ages clustering around 32–29 Ma are interpreted as a distinctive age population and all the other ages in the time interval between 36 and 33 Ma are assigned to a second, older one, the calculation of weighted average ages yields  $34.16 \pm 1.22$  Ma

for the older and  $30.32 \pm 0.49$  Ma for the younger age population, as depicted by gray bars in Figure 9.

### 6.3. Conclusions Regarding the Age Interpretation

[48] Apparent ages in the 45–37 Ma range, with a weighted average age of  $41.23 \pm 1.22$  Ma, are interpreted to represent the timing of peak pressure conditions. This interpretation is supported by the fact that isolated phengites exclusively yield older ages compared to phengite-chlorite aggregates that replace carpholite and, by microstructural observations pointing to coeval trapping in quartz porphyroclasts of such isolated phengites (3.30–3.40 Si pfu) and fibers of Fe-Mg carpholite under the same metamorphic conditions, i.e., under peak pressure conditions.

[49] The retrograde path is basically pressure controlled, being characterized by isothermal or only slightly cooling decompression [Bousquet *et al.*, 1998, 2002; Jolivet *et al.*, 1998; Wiederkehr *et al.*, 2008]. Because Fe-Mg carpholite and coexisting high-pressure phengite were destabilized to

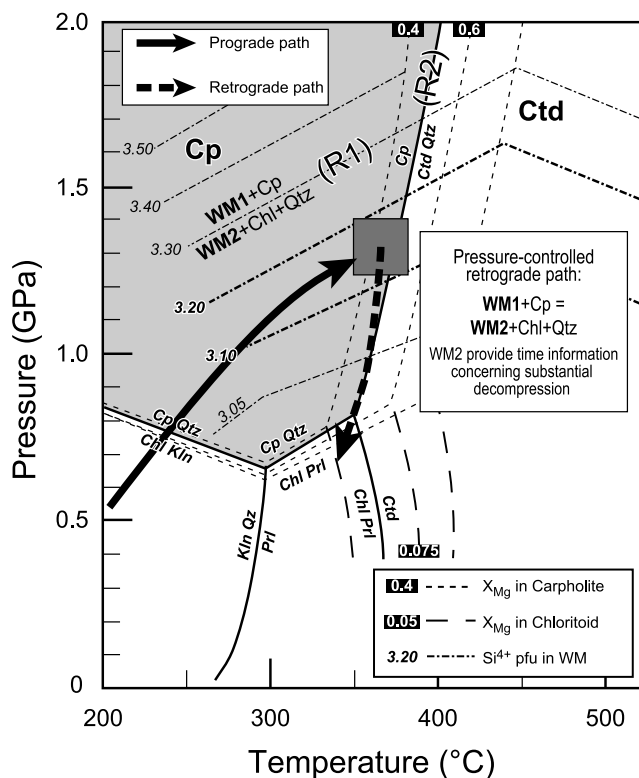


**Figure 10.** P-T diagram for low-grade carpholite-bearing HP/LT metasediments showing the successive phengite generations formed during the P-T evolution. Phengite may either coexist together with Fe-Mg carpholite (generally characterized by higher Si contents, i.e., 3.3–3.4 Si pfu, white mica 1) or, alternatively, may be formed by the breakdown of Fe-Mg carpholite due to substantial decompression (generally found in pseudomorphs after carpholite and characterized by lower Si contents, i.e., 3.2 Si pfu, white mica 2). P-T diagram and calculated Si isopleths are taken after *Bousquet et al.* [2008]; due to considerable interlayer deficiency in the studied low-grade HP/LT metasediments the Si content pfu representing the celadonite content was calculated following *Bousquet et al.* [2002]. The following mineral abbreviations used: WM, white mica; Qtz, quartz; Prl, pyrophyllite; Kln, kaolinite; Ctd, chloritoid.

muscovite, chlorite and quartz (Figure 10) [*Oberhänsli et al.*, 1995; *Bousquet et al.*, 2002] the apparent ages recorded in white mica associated with chlorite, which are interpreted to represent pseudomorphs after carpholite, provide information on the timing of decompression. Apparent ages of this group cover a wide time interval ranging from 36 to 29 Ma, except for sample VAL 0580 that will be discussed separately below. This time interval can possibly be subdivided into two distinct populations, an older one in the range of 36–33 Ma yielding an average age of  $34.16 \pm 1.22$  Ma and a younger one between 32 and 29 Ma with a weighted average age of  $30.32 \pm 0.49$  Ma (depicted by the gray bars in Figure 9).

[50] Sample VAL 0580, however, is characterized by significantly younger and well-defined apparent ages in the

range of 28–23 Ma, with a weighted average age of  $25.40 \pm 0.45$  Ma. In view of its distinctly different microstructure (Figures 5c and 5d) it is most probable that partial recrystallization and/or exchange reactions along the retrograde metamorphic evolution did induce chemical reequilibration and isotopic resetting in this particular sample (see discussion by *Villa* [1998]). Such reequilibration associated with isotopic resetting of white mica might possibly have been enhanced by deformation [see, e.g., *Müller et al.*, 1999]. Sample VAL 0580 originates from a polyphase folded quartz-calcite segregation pervasively affected by D3 deformation. Hence we tentatively relate the weighted average age of  $25.40 \pm 0.45$  Ma to D3 deformation (Domleschg phase), being aware that such an interpretation is highly speculative.

[51] All the investigated biotite samples yield significantly younger apparent ages compared to ages obtained on white mica. Also, all investigated biotite domains give consistent ages that cluster in a range between 18 and 15.5 Ma. This is consistent with the fact that biotite is related to a single metamorphic event represented by Barrow-type overprint that only affects the southwestern part of the study area and postdates D3 deformation (Figure 1b) [*Wiederkehr et al.*, 2008]. The ages are also consistent with recently published  $^{40}\text{Ar}/^{39}\text{Ar}$  ages of 19–16 Ma obtained by isotopic investigations on white mica and biotite for the Lucomagno and Pizzo Molare areas [*Allaz*, 2008]. The published monazite U-Pb ages of 19–18 Ma [*Janots et al.*, 2009] are interpreted to reflect equilibrations close to the “gamet-in” isograd, i.e., very near the thermal peak of metamorphism. As also shown by *Allaz* [2008] the lower apparent ages obtained on biotite are most probably due to late reequilibration, i.e., chloritization of biotite associated with isotopic resetting along the retrograde path.

#### 6.4. Comparison With Previously Published Isotopic and Fission Track Data

##### 6.4.1. White Mica Ages

[52] The age of  $41.23 \pm 1.22$  Ma that we interpret to date HP/LT metamorphism in the Valaisan domain at the NE rim of the Lepontine dome appears reasonable when compared to the very few other available geochronological investigations of subduction-related metamorphism performed in units that belong to the Valaisan paleogeographical domain. For example, 46–39 Ma have been obtained within the western Lepontine (Antrona ophiolites) [*Liati et al.*, 2005]. 45–40 Ma were postulated for the Tauern Eclogite Zone [*Ratschbacher et al.*, 2004]; albeit younger ages were postulated for the same high-pressure event in that same area based on an unconvincing interpretation of Rb-Sr white mica ages [*Glodny et al.*, 2005] and on Ar-Ar dating of white mica in eclogites [*Kurz et al.*, 2008] indicating that eclogite facies conditions prevailed into the Oligocene (ca. 32 Ma). Our ages obtained for HP/LT metamorphism are somewhat older than the 40–35 Ma age range previously postulated for the Engadine window [*Bertle*, 2004], but again considerably older than suggested by Rb-Sr and Ar-Ar white mica studies performed in metasediments exposed around Petit St. Bernard area that yielded ages around 34–27 Ma [*Freeman et al.*, 1998; *Cannic et al.*, 1999].

[53] Geochronological investigations performed in the tectonically higher and more internal Briançonnais domain revealed 46 Ma for subduction-related HP/LT metamorphism in the Suretta nappe [Challandes *et al.*, 2003]. A recent study based on Rb-Sr geochronology yield ages near 50 Ma for subduction-related deformation in the Piemont-Liguria oceanic domain in the study area (Platta nappe [Bachmann *et al.*, 2009]). These older ages are in agreement with the common assumption that the timing of high-pressure metamorphism propagates toward the foreland and hence progressively becomes younger toward more external units. Such a view is further supported by ages obtained within a younger 43–35 Ma time interval interpreted to date high-pressure metamorphism in the relatively more external Adula nappe complex [Gebauer *et al.*, 1992; Becker, 1993; Gebauer, 1996; Brouwer *et al.*, 2005; Nagel, 2008], a tectonic unit interpreted as representing the distal European margin.

[54] The timing of the intrusion of the Bergell pluton at 32–30 Ma [von Blanckenburg, 1992] still represents the hardest constraint for indirectly dating the tectonometamorphic evolution of the Alps. This magmatic event postdates a first nappe-refolding event (Niemet-Beverin phase) [Schmid *et al.*, 1990; Schreurs, 1993] that followed the closure of the Valaisan Ocean and the subduction of the European continental margin (Adula nappe complex). The first part of the decompression path at around 36–33 Ma (with the corresponding weighted average age of  $34.16 \pm 1.22$  Ma) as well as the HP granulites of the Gruf complex (southern Adula, 33 Ma) [Schmitz *et al.*, 2009] predates the Bergell intrusion. Early Oligocene decompression seems to be a regional feature not restricted to the Valaisan metasediments and is probably due to syncollisional exhumation, which is in line with the onset of erosion in the Alps and of massive sediment deposition in the Alpine foredeeps at that time [see e.g., Hermann *et al.*, 2006; Glodny *et al.*, 2008c]. This older exhumation is associated with pervasive recrystallization of white mica, related to the breakdown of Fe-Mg carpholite (Figure 10) and the formation of the main foliation during D2 nappe stacking [Wiederkehr *et al.*, 2008]. It predates D3 and overprints the D1 high-pressure event. Hence, this main foliation was formed during the retrograde evolution while high-pressure relics, and associated isotopic ages, are only selectively preserved within the carpholite-bearing quartz-calcite veins. We conclude that it is very likely that the apparent ages determined by stepwise heating techniques of white mica separated from whole rock samples only provide information on the retrograde evolution during substantial decompression in the 36–34 Ma time interval. Also the ages obtained by Bertle [2004], recorded on white mica of the rock matrix close to carpholite-bearing quartz-calcite veins (40–35 Ma, giving a plateau age of 35.6 Ma), may fall into this same category of ages and reflect rather the timing of substantial decompression than peak pressure conditions.

[55] The younger post peak pressure event postulated for the 32–29 Ma age interval, with a weighted average age of  $30.32 \pm 0.49$  Ma, would be more or less contemporaneous with the intrusion of the Bergell pluton [von Blanckenburg,

1992]. We interpret it to represent a separate greenschist facies overprint that occurred after a first stage of substantial decompression. Interestingly, in situ Th-Pb measurements on allanite by SHRIMP from individual samples from the northern Lepontine (Piora and Lucomagno area) also yield ages between 32 and 29 Ma [Janots *et al.*, 2009]. Allanite generally appears at 400–450°C and is therefore indicative for greenschist facies metamorphic conditions [e.g., Janots *et al.*, 2006]. All this indicates that the 32–29 Ma event probably reflects a significant stage of greenschist facies metamorphic overprint during the formation of the Alpine orogenic belt.

#### 6.4.2. Biotite

[56] We relate the biotite ages, clustering in the range between 18 and 15.5 Ma, to Barrovian metamorphism in the NE part of the Lepontine dome. There are numerous other isotopic data available for the northern Lepontine with K-Ar, Ar-Ar and Rb-Sr ages obtained from white mica and biotite ranging from 42 all the way to 14 Ma (see reviews given by Hunziker *et al.* [1992] and Steck and Hunziker [1994, and references therein]). Classical K-Ar and Ar-Ar ages obtained by pioneering isotopic investigations in the northern Lepontine yielded 25–16 Ma for white mica and 17–14 Ma for biotite [Armstrong *et al.*, 1966; Purdy and Jäger, 1976; Hunziker *et al.*, 1986]. These early pioneering isotopic investigations mainly focused on basement units, which are generally characterized by a polyphase metamorphic evolution and where the interpretation of the obtained ages is hampered by inheritance from pre-Alpine metamorphic stages. To avoid such problems recent isotopic investigations were performed exclusively in Mesozoic metasediments that only suffered Alpine metamorphic overprint [Allaz, 2008; Janots *et al.*, 2009]. For the northeastern Lepontine dome, i.e., area around Val Piora-Lukmanier-Pizzo Molare, these recent Ar-Ar investigations revealed ages of 19–16 Ma for muscovite and 18–16 for biotite [Allaz, 2008]. The obtained Ar-Ar ages were confirmed by in situ SHRIMP U-Pb dating of monazite yielding an age between 19 and 18 Ma for the same area, which is interpreted to reflect conditions near the thermal peak of metamorphism [Janots *et al.*, 2009], in perfect agreement with our results. In summary, these recent investigations, combined with the results of this study, unambiguously demonstrate that Barrow-type amphibolite facies metamorphism in the northern Lepontine dome is surprisingly young, i.e., post 20 Ma. Interestingly the presented results coincide just perfectly with ages reported for amphibolite facies conditions in the Western Tauern window [Glodny *et al.*, 2008c], indicating that Barrovian thermal overprint is indeed a rather young and late stage event of the orogenic evolution the Alpine belt.

[57] Our biotite  $^{40}\text{Ar}/^{39}\text{Ar}$  isotopic ages are also in agreement with fission track dating on apatite and zircon related to the late stages of exhumation. In the northern Lepontine dome the zircon cooling central ages (at  $\sim 290^\circ\text{C}$ ) [Tagami and Shimada, 1996] vary between 14 and 12.2 Ma while the apatite central ages (at  $110\text{--}60^\circ\text{C}$ ) [Hurford, 1990] are in the range of 9–5 Ma [Hurford, 1986; Michalski and Soom, 1990; Vernon *et al.*, 2008]. Within our study area (i.e., southern

Gotthard massif near Lukmanier pass and frontal part of the Adula nappe complex around Olivone; Figure 1b) recent investigations yielded zircon and apatite fission track central ages of 10–9 Ma and 7.5–6.5 Ma, respectively [Janots *et al.*, 2009].

## 6.5. Implications Regarding the Tectonometamorphic Evolution of the Valaisan and Adjacent Units

[58] The new geochronological data presented in this study further constrain the timing of the subduction-collision transition in the central Alps preserved in the Valaisan domain as summarized in Figure 11. In the following, we integrate the isotopic ages into the geodynamic model recently presented by *Wiederkehr et al.* [2008] and make an attempt to construct a complete P-T-d-t path for the high-pressure metasedimentary units NE of the Lepontine dome. The numbering and associated names of deformation events are those introduced by *Wiederkehr et al.* [2008].

### 6.5.1. Eocene Sediment Accretion and Subduction, 42–40 Ma, D1 Safien Phase

[59] The huge pile of Valaisan Bündnerschiefer of the Grisons area, including the Engadine window, are generally interpreted to have formed an accretionary wedge during Cenozoic subduction of the Valaisan Ocean followed by the subduction of the adjacent distal European margin beneath the Briançonnais microcontinent that was previously accreted to the Austroalpine upper plate. The age of the sediments within this accretionary wedge ranges from 50 Ma (Valaisan domain) [Steinmann, 1994] to some 40 Ma (more external Sardona unit) [Lihou and Allen, 1996]. The high-pressure relics are restricted to synmetamorphic quartz-calcite segregations formed during the first deformation event D1 (Safien phase) coeval with the HP/LT metamorphic event. Our isotopic ages on phengite, associated with Fe-Mg carpholite, revealed a weighted average age of  $41.23 \pm 1.22$  Ma for this peak pressure (350–400°C and 1.2–1.4 GPa) D1 event (Figure 11). The proposed time interval for high-pressure metamorphism is in accordance with the available stratigraphical constraints and the recognition of a Paleocene-Eocene radiolaria species in carpholite-bearing metasediments in Safiental [Bousquet *et al.*, 2002].

### 6.5.2. Nappe Stacking and Decompression Stage, 36–33 Ma, D2 Ferrera Phase

[60] Nappe stacking in the Lepontine was associated with substantial decompression of the blueschist facies rocks (Figure 11). The observation that carpholite is mainly destabilized by a mineral reaction producing white mica, chlorite and quartz points toward decompression under nearly isothermal or slightly cooling conditions (Figure 10). All apparent ages in this 36–33 Ma time interval were recorded on white mica intimately associated with chlorite and inter-

preted to replace carpholite during decompression that is contemporaneous with D2 (Ferrera phase) nappe stacking. The proposed 36–33 Ma age range supports the interpretation of *Wiederkehr et al.* [2008] that the D2 Ferrera nappe stacking phase in the Valaisan postdates earlier stages of nappe stacking related to this same Ferrera phase as defined for the Briançonnais domain, where 46 Ma were reported for nappe stacking [Challandes *et al.*, 2003].

### 6.5.3. Greenschist Facies Event, 32–29 Ma

[61] This event, recorded within a second population of phengites picked in chlorite-phengite associations replacing Fe-Mg carpholite and yielding apparent ages in the range of 32–29 Ma (weighted average age of  $30.32 \pm 0.49$  Ma) coincides with an event recorded by Th-Pb dating of allanite that also dates greenschist facies conditions further west in the Lukmanier/Val Piora area [Janots *et al.*, 2009]. The geodynamical significance of this greenschist facies overprint associated with isotopic resetting is not clear at this stage. The event predates the D3 deformation that we correlate with the so-called Domleschg phase, which hence postdates the Bergell intrusion [Wiederkehr *et al.*, 2008]. Possibly, the accretion of distal European margin to the orogenic wedge led to the relaxation of subduction-related downfolded isotherms by providing additional heat supply caused by high radiogenic heat production.

### 6.5.4. First Nappe Refolding Event, ~25 Ma, D3 Domleschg Phase

[62] The D3 (Domleschg phase) nappe refolding event substantially modified the nappe stack in the investigated area and produced tight to isoclinal megafolds with amplitudes up to some 10 km, particularly the most prominent Lunschania antiform (Figures 1b and 11). D3 deformation postdates the ascent and emplacement of the Bergell pluton south of the working area [e.g., Schmid *et al.*, 1996] (Figure 11) and overprints the previously established greenschist facies event, as is independently evidenced by isotherms related to this greenschist facies event that are folded around the Lunschania antiform [Wiederkehr, 2009]. D3 deformation is associated with ongoing accretion of continental basement (e.g., Lucomagno-Leventina nappe and Gotthard-“massif”; Figure 11). Based on the significantly younger apparent ages (weighted average age of  $25.40 \pm 0.45$  Ma) found in the sample from Valsertal (sample VAL 0580), affected by pervasive D3 deformation and showing unambiguously different microtexture, we tentatively correlate these recorded apparent age with the timing of D3 deformation, being aware that this is speculative.

### 6.5.5. Miocene Barrow-Type Thermal Overprint, 19–18 Ma

[63] Barrovian overprint of the southwestern part of the study area represents a separate and younger heating event

---

**Figure 11.** Summary of age data, dating of P-T loops and tentative geodynamic evolution based on the interpretation of the isotopic data obtained for the study area. The sketches of the geodynamic stages are modified after Schmid *et al.* [1996]. This summary is also based on a recent model proposed by *Wiederkehr et al.* [2008]. Additional geochronological data from the study area were taken from (1) Th-Pb dating of allanite by Janots *et al.* [2009], (2) U-Pb dating of monazite by Janots *et al.* [2009], (3)  $^{40}\text{Ar}/^{39}\text{Ar}$  ages of white mica by Allaz [2008], (4)  $^{40}\text{Ar}/^{39}\text{Ar}$  ages of biotite by Allaz [2008], (5) zircon fission track ages of Janots *et al.* [2009], (6) apatite fission track ages of Janots *et al.* [2009].

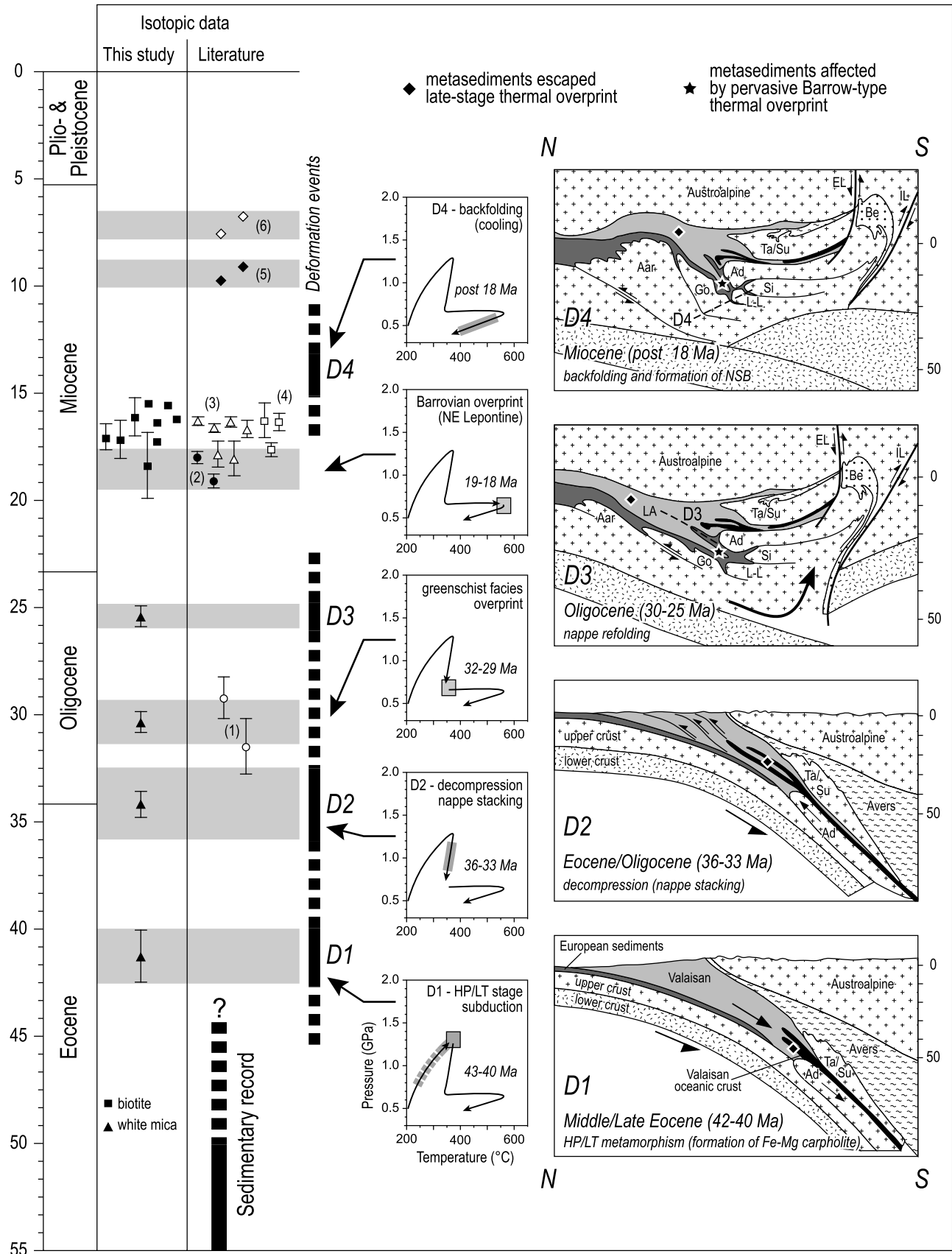


Figure 11

that initiated during a tectonically quiescent phase and that clearly postdates D3 deformation [Wiederkehr *et al.*, 2008]. This is demonstrated by the isotherms related to this Barrovian metamorphism that are seen to crosscut the D3 Lunschania antiform [Wiederkehr, 2009]. This event is recorded by the apparent ages of our biotite domains that cluster in the 18–15.5 Ma range; due to some retrograde chloritization of biotite we prefer the published monazite U-Pb ages of 19–18 Ma [Janots *et al.*, 2009] for dating peak temperatures during this event (Figure 11). Barrow-type thermal overprint in the NE Lepontine is caused by the accretion of vast amounts of European continental crust (forming the present-day Lepontine dome) that provides high radiogenic heat production responsible for amphibolite facies metamorphism [e.g., Goffé *et al.*, 2003; Bousquet *et al.*, 2008] (and discussion by Wiederkehr *et al.* [2008]).

#### 6.5.6. Back Folding in the Northern Steep Belt, Post-18 Ma, D4 Chièra Phase

[64] Barrow-type amphibolite facies mineral assemblages have been severely deformed by a subsequent late stage nappe refolding event that is associated with the formation of the Northern Steep Belt within the Penninic nappe stack and which is only very well developed west of our study area [Milnes, 1974]. There, a relatively tight synform, the Chièra synform, brings the nappe stack into an overturned, steeply north dipping position, while in our area (see profile in Figure 11) such D4 back folding is less severe. Since this D4 Chièra phase deformation outlasted Barrovian metamorphic overprint it must be very young (i.e., post-18 Ma), most probably contemporaneous with the north directed thrusting in the Aar massif in the more external parts of the Alps and imbrications within the Subalpine molasse. Recently published isotopic data on a greenschist facies shear zone of the Aar Massif (External Crystalline Massif) report 21–17 Ma [Challandes *et al.*, 2008] and may be correlated with this D4 deformation. The zircon fission track ages of 10–9 Ma, as well as apatite fission track ages of 7.5–6.5 Ma [Janots *et al.*, 2009], indicate the final stages of the P-T path, i.e., the timing of cooling below some 200–330°C for zircon, and 70–120°C for apatite due to erosional unroofing that followed the thrusting of the external massifs.

## 7. Conclusions

[65] The new age constraints obtained for the HP/LT metasedimentary units of the Valaisan and adjacent European domains provide valuable information regarding the timing of the transition from subduction-related peak high-pressure metamorphism to decompression and finally to a collision-related and second Barrow-type thermal overprint.

[66] Phengites, texturally associated with Fe-Mg carpholite yield apparent ages of 42–40 Ma interpreted as dating HP/LT conditions at 350–400°C and 1.2–1.4 GPa (D1, Safien phase). Age constraints belonging to the evolution during or immediately after decompression were revealed by white mica intimately associated with chlorite occurring in pseudomorphs after carpholite and yield two populations: an earlier one clusters at 36–33 Ma, a later one at 32–29 Ma,

respectively. We relate the older retrograde stage to substantial decompression during which carpholite was destabilized by the reaction producing white mica, chlorite and quartz during D2 nappe stacking (Ferrera phase). The younger population is interpreted as related to greenschist facies metamorphism established at the end of decompression. Additionally, the white mica data also reveal a coherent apparent age cluster at ~25 Ma whose significance is yet not clear; a correlation with D3 deformation (Domleschg phase) is proposed. The still younger apparent ages recorded by biotite, only occurring in the SW part of the study area and clearly related to collision-related amphibolite facies metamorphism of the northeastern Lepontine dome, date a second and distinct pervasive Barrovian overprint and cluster around 18–16 Ma.

[67] The presented isotopic ages support and further constrain the relative chronology of the tectonometamorphic evolution presented by Wiederkehr *et al.* [2008] and Wiederkehr [2009] established on the basis of relationships between metamorphism and deformation. The consistency of the presented isotopic results presented in this study with such other and independent data indicates that an overall contamination by excess argon, as well as diffusional loss of  $^{40}\text{Ar}^*$ , can be ruled out, or is at least only of minor importance in the case of our study. Apparent ages deduced by the investigation of white mica are interpreted to represent formation and/or crystallization ages under temperature conditions that never exceeded 400°C, hence far below the “closure temperature” of 500–550°C estimated for white mica [Di Vincenzo *et al.*, 2001, and references therein]. The apparent ages of biotite, that yield slightly younger ages than the assumed thermal peak (19–18 Ma) [Janots *et al.*, 2009], probably represent recrystallization ages that are affected by partial isotopic resetting during retrograde mineral reactions such as the chloritization of biotite which immediately followed peak temperature conditions [see also Allaz, 2008].

[68] The recorded isotopic data reveal a significant time gap in the order of some 20 Ma between the subduction-related HP/LT event (42–40 Ma) and the later collision-related MP/MT Barrovian overprint (19–18 Ma). This substantial time gap, together with the age constraints on white mica reflecting the retrograde metamorphic evolution of the HP/LT stage, support the notion of a polymetamorphic evolution associated with a bimodal P-T path [Wiederkehr *et al.*, 2008]. Amphibolite facies Barrow-type overprint of the NE Lepontine dome represents a clearly separated heating pulse that postdates isothermal decompression after the early high-pressure stage. This considerable time interval is in accordance with the interpretation that it is the accretion of vast amounts of European continental crust (forming the present-day Lepontine dome) that provides high radiogenic heat production responsible for amphibolite facies metamorphism [e.g., Bousquet *et al.*, 2008], being an entirely conductive and therefore rather slow process.

[69] **Acknowledgments.** Excellent preparation of samples by W. Tschudin (Basel University) and C. Fischer (Potsdam University) is gratefully acknowledged. M. Timmerman from University of Potsdam is thanked for the help with sample selection and preparation as well as

providing basic literature concerning  $^{40}\text{Ar}/^{39}\text{Ar}$  dating techniques. O. Appelt and D. Rhede from the GeoForschungsZentrum Potsdam are thanked for their help with microprobe analyses. The introduction to the  $^{40}\text{Ar}/^{39}\text{Ar}$  noble gas laboratory as well as the supporting field visit of A. Riemann (Potsdam University) is highly appreciated. J.-P. Hürzeler is thanked for the help with SEM investigations. We also thank the two reviewers I. M. Villa

and J. Glodny for their constructive comments and suggestions for improving this paper, and the editor in chief O. Oncken and the Associate Editor L. Ratschbacher for their careful handling of the manuscript. Funding by the Swiss National Science Foundation (project NF-200020-113585 and precursor project NF-200020-103585) is gratefully acknowledged.

## References

- Agard, P., L. Jolivet, and B. Goffé (2001), Tectonometamorphic evolution of the Schistes Lustrés complex: Implications for the exhumation of HP and UHP rocks in the Western Alps, *Bull. Soc. Geol. Fr.*, *172*, 617–636, doi:10.2113/172.5.617.
- Agard, P., P. Monié, L. Jolivet, and B. Goffé (2002), Exhumation of the Schistes Lustrés complex: In situ laser probe  $^{40}\text{Ar}/^{39}\text{Ar}$  constraints and implications for the Western Alps, *J. Metamorph. Geol.*, *20*, 599–618, doi:10.1046/j.1525-1314.2002.00391.x.
- Allaz, J. (2008), Metamorphic evolution in the northern central Alps: Linking  $^{39}\text{Ar}/^{40}\text{Ar}$  dating with thermobarometry, Ph.D. thesis, Univ. Bern, Bern.
- Armstrong, R. L., E. Jäger, and P. Eberhardt (1966), A comparison of K-Ar and Rb-Sr ages on Alpine biotites, *Earth Planet. Sci. Lett.*, *1*, 13–19, doi:10.1016/0012-821X(66)90097-5.
- Bachmann, R., J. Glodny, O. Oncken, and W. Seifert (2009), Abandonment of the South Penninic-Austroalpine palaeosubduction zone, central Alps, and shift from subduction erosion to accretion: Constraints from Rb/Sr geochronology, *J. Geol. Soc.*, *166*, 217–231, doi:10.1144/0016-76492008-024.
- Balogh, K., and I. Dunkl (2005), Argon and fission track dating of Alpine metamorphism and basement exhumation in the Sopron Mts. (Eastern Alps, Hungary): Thermochronology or mineral growth?, *Mineral. Petrol.*, *83*, 191–218, doi:10.1007/s00710-004-0066-0.
- Baumer, A., J. D. Frey, W. Jung, and A. Uhr (1961), Die Sedimentbedeckung des Gotthard-Massivs zwischen oberen Bleniol und Lugnez (Vorläufige Mitteilung), *Eclogae Geol. Helv.*, *54*, 478–491.
- Beath, P. (1967), Die Ophiolite der Zone von Zermatt-Saas Fee, *Beitr. Geol. Kt. Schweiz*, *132*, 130 pp., Kümmerly und Frey, Bern.
- Becker, H. (1993), Garnet peridotite and eclogite Sm-Nd mineral ages from the Lepontine dome (Swiss Alps)—New evidence for Eocene high-pressure metamorphism in the central Alps, *Geology*, *21*, 599–602, doi:10.1130/0091-7613(1993)021<0599:GPAESN>2.3.CO;2.
- Berger, A., and R. Bousquet (2008), Subduction related metamorphism in the Alps: Review of isotopic ages based on petrology and their geodynamic consequences, in *Tectonic Aspects of the Alpine-Dinaride-Carpathian System*, edited by S. Siegesmund et al., *Geol. Soc. Spec. Publ.*, *298*, 117–144.
- Berger, A., I. Mercolli, and M. Engi (2005), The central Lepontine Alps: Notes accompanying the tectonic and petrographic map sheet Sopra Ceneri (1:100,000), *Schweiz. Mineral. Petrogr. Mitt.*, *85*, 109–146.
- Bertle, R. J. (2004), Zur Geologie des Piz Mundin-Gebietes (Engadiner Fenster, Österreich-Schweiz): Stratigraphie, Geochronologie, Strukturen, Ph.D. thesis, Univ. Wien, Vienna.
- Bousquet, R., B. Goffé, P. Henry, X. Le Pichon, and C. Chopin (1997), Kinematic, thermal and petrological model of the central Alps: Lepontine metamorphism in the upper crust and eclogitisation of the lower crust, *Tectonophysics*, *273*, 105–127, doi:10.1016/S0040-1951(96)00290-9.
- Bousquet, R., R. Oberhänsli, B. Goffé, L. Jolivet, and O. Vidal (1998), High-pressure-low-temperature metamorphism and deformation in the Bündnerschiefer of the Engadine window: Implications for the regional evolution of the eastern central Alps, *J. Metamorph. Geol.*, *16*, 657–674, doi:10.1111/j.1525-1314.1998.00161.x.
- Bousquet, R., B. Goffé, O. Vidal, R. Oberhänsli, and M. Patriat (2002), The tectono-metamorphic history of the Valaisan domain from the Western to the central Alps: New constraints on the evolution of the Alps, *Geol. Soc. Am. Bull.*, *114*, 207–225, doi:10.1130/0016-7606(2002)114<0207:TTMHOT>2.0.CO;2.
- Bousquet, R., R. Oberhänsli, B. Goffé, M. Wiederkehr, F. Koller, S. M. Schmid, R. Schuster, M. Engi, A. Berger, and G. Martinotti (2008), Metamorphism of metasediments at the scale of an orogen: A key to the Tertiary geodynamic evolution of the Alps, in *Tectonic Aspects of the Alpine-Dinaride-Carpathian System*, edited by S. Siegesmund et al., *Geol. Soc. Spec. Publ.*, *298*, 393–411.
- Brouwer, F. M., T. Burri, M. Engi, and A. Berger (2005), Eclogite relics in the central Alps: PT-evolution, Lu-Hf ages and implications for formation of tectonic mélange zones, *Schweiz. Mineral. Petrogr. Mitt.*, *85*, 147–174.
- Bucher, S. (2003), The Briançonnais units along the ECORS-CROP transect (Italian-French Alps): Structures, metamorphism and geochronology, Ph.D. thesis, Univ. Basel, Basel, Switzerland.
- Camacho, A., J. K. W. Lee, B. J. Hensen, and J. Braun (2005), Short-lived orogenic cycles and the eclogitization of cold crust by spasmodic hot fluids, *Nature*, *435*, 1191–1196, doi:10.1038/nature03643.
- Cannic, S., J.-L. Mugnier, and J.-M. Lardeaux (1999), Neogene extension in the western Alps, in *3rd Workshop on Alpine Geological Studies*, edited by G. Gosso et al., *Mem. Sci. Geol. Padova*, *51*, 33–45.
- Chadwick, B. (1968), Deformation and metamorphism in the Lukmanier region, central Switzerland, *Geol. Soc. Am. Bull.*, *79*, 1123–1150, doi:10.1130/0016-7606(1968)79[1123:DAMITL]2.0.CO;2.
- Challandes, N., D. Marquer, and I. M. Villa (2003), Dating the evolution of C-S microstructures: A combined  $^{40}\text{Ar}/^{39}\text{Ar}$  step-heating and UV laserprobe analysis of the Alpine Roffna shear zone, *Chem. Geol.*, *197*, 3–19, doi:10.1016/S0009-2541(02)00354-6.
- Challandes, N., D. Marquer, and I. M. Villa (2008), P-T-t modelling, fluid circulation, and  $^{39}\text{Ar}/^{40}\text{Ar}$  and Rb-Sr mica ages in the Aar Massif shear zones (Swiss Alps), *Swiss J. Geosci.*, *101*, 269–288, doi:10.1007/s00015-008-1260-6.
- Chinner, G. A., and J. E. Dixon (1973), Some high-pressure parageneses of Allalin Gabbro, Valais, Switzerland, *J. Petrol.*, *14*, 185–202.
- Chopin, C., and H. Maluski (1980),  $^{40}\text{Ar}/^{39}\text{Ar}$  dating of high-pressure metamorphic micas from the Gran Paradiso area (Western Alps)—Evidence against the blocking temperature concept, *Contrib. Mineral. Petrol.*, *74*, 109–122, doi:10.1007/BF01131997.
- Chopin, C., and P. Monié (1984), A unique magnesiochloritoid-bearing, high-pressure assemblage from the Monte-Rosa, Western Alps—Petrologic and  $^{40}\text{Ar}/^{39}\text{Ar}$  radiometric study, *Contrib. Mineral. Petrol.*, *87*, 388–398, doi:10.1007/BF00381295.
- Clauer, N. (1980), Strontium and argon isotopes in naturally weathered biotites, muscovites and feldspars, *Chem. Geol.*, *31*, 325–334, doi:10.1016/0009-2541(80)90094-7.
- Clauer, N., J. R. O'Neil, and C. Bonnotcourtois (1982), The effect of natural weathering on the chemical and isotopic compositions of biotites, *Geochim. Cosmochim. Acta*, *46*, 1755–1762, doi:10.1016/0016-7037(82)90115-6.
- Di Vincenzo, G., B. Ghiribelli, G. Giorgetti, and R. Palmeri (2001), Evidence of a close link between petrology and isotope records: Constraints from SEM, EMP, TEM and in situ  $^{40}\text{Ar}/^{39}\text{Ar}$  laser analyses on multiple generations of white micas (Lantermann Range, Antarctica), *Earth Planet. Sci. Lett.*, *192*, 389–405, doi:10.1016/S0012-821X(01)00454-X.
- Di Vincenzo, G., R. Carosi, and R. Palmeri (2004), The relationship between tectono-metamorphic evolution and argon isotope records in white mica: Constraints from in situ  $^{40}\text{Ar}/^{39}\text{Ar}$  laser analysis of the Variscan basement of Sardinia, *J. Petrol.*, *45*, 1013–1043, doi:10.1093/petrology/egh002.
- Di Vincenzo, G., S. Tonarini, B. Lombardo, D. Castelli, and L. Ottolini (2006), Comparison of  $^{40}\text{Ar}/^{39}\text{Ar}$  and Rb-Sr data on phengites from the UHP Brossasco-Isasca unit (Dora Maira Massif, Italy): Implications for dating white mica, *J. Petrol.*, *47*, 1439–1465, doi:10.1093/petrology/egl018.
- Dodson, M. H. (1973), Closure temperature in cooling geochronological and petrological systems, *Contrib. Mineral. Petrol.*, *40*, 259–274, doi:10.1007/BF00373790.
- Engi, M., C. S. Todd, and D. R. Schmatz (1995), Tertiary metamorphic conditions in the eastern Lepontine Alps, *Schweiz. Mineral. Petrogr. Mitt.*, *75*, 347–369.
- Ernst, W. G., and G. V. Dal Piaz (1978), Mineral parageneses of eclogitic rocks and related mafic schists of the Piemonte ophiolite nappe, Breuil-St. Jacques area, Italian Western Alps, *Am. Mineral.*, *63*, 621–640.
- Etter, U. (1987), Stratigraphische und strukturelle geologische Untersuchungen im gotthardmassivischen Mesozoikum zwischen dem Lukmanierpass und der Gegend von Ilanz, Ph.D. thesis, Univ. Bern, Bern.
- Florineth, D., and N. Froitzheim (1994), Transition from continental to oceanic basement in the Tasna nappe (Engadine window, Graubünden, Switzerland): Evidence for Early Cretaceous opening of the Valaisan Ocean, *Schweiz. Mineral. Petrogr. Mitt.*, *74*, 437–448.
- Foland, K. A. (1979), Limited mobility of argon in a metamorphic terrain, *Geochim. Cosmochim. Acta*, *43*, 793–801, doi:10.1016/0016-7037(79)90219-9.
- Fox, J. S. (1975), Three-dimensional isograds from the Lukmanier-Pass, Switzerland, and their tectonic significance, *Geol. Mag.*, *112*, 547–564, doi:10.1017/S0016756800038966.
- Freeman, S. R., R. W. H. Butler, R. A. Cliff, S. Inger, and T. A. C. Barnicoat (1998), Deformation migration in an orogen-scale shear zone array: An example from the basal Briançonnais thrust, internal Franco-Italian Alps, *Geol. Mag.*, *135*, 349–367, doi:10.1017/S0016756898008693.
- Frey, M. (1969), Die Metamorphose des Keupers vom Tafeljura bis zum Lukmanier-Gebiet, *Beitr. Geol. Kt. Schweiz*, *137*, 160 pp., Kümmerly und Frey, Bern.
- Frey, M. (1974), Alpine metamorphism of pelitic and marly rocks of the Central Alps, *Schweiz. Mineral. Petrogr. Mitt.*, *54*, 489–506.
- Frey, M. (1978), Progressive low-grade metamorphism of a black shale formation, Central Swiss Alps, with special reference to Pyrophyllite and Margarite bearing assemblages, *J. Petrol.*, *19*, 95–135.

- Frey, M., and R. Ferreiro Mählmann (1999), Alpine metamorphism of the central Alps, *Schweiz. Mineral. Petrogr. Mitt.*, **79**, 135–154.
- Frisch, W. (1979), Tectonic progradation and plate tectonic evolution of the Alps, *Tectonophysics*, **60**, 121–139, doi:10.1016/0040-1951(79)90155-0.
- Froitzheim, N., S. M. Schmid, and M. Frey (1996), Mesozoic paleogeography and the timing of eclogite-facies metamorphism in the Alps: A working hypothesis, *Eclogae Geol. Helv.*, **89**, 81–110.
- Froitzheim, N., J. Pleuger, S. Roller, and T. Nagel (2003), Exhumation of high- and ultrahigh-pressure metamorphic rocks by slab extraction, *Geology*, **31**, 925–928, doi:10.1130/G19748.1.
- Gebauer, D. (1996), A P-T-t path for a high-pressure ultramafic rock-association and their felsic country-rocks based on SHRIMP-dating of magmatic and metamorphic zircon domains. Example: Alpe Arami (central Swiss Alps), in *Reading the Isotope Code, Geophys. Monogr. Ser.*, vol. 95, edited by A. Hart and S. R. Basu, pp. 307–328, AGU, Washington, D. C.
- Gebauer, D., M. Grünfelder, G. Tilton, V. Trommsdorff, and S. M. Schmid (1992), The geodynamic evolution of garnet-peridotites, garnet-pyroxenites and eclogites of Alpe Arami and Cima di Gagnone (central Alps) from Early Proterozoic to Oligocene, *Schweiz. Mineral. Petrogr. Mitt.*, **72**, 107–111.
- Glodny, J., U. Ring, A. Kühn, P. Gleissner, and G. Franz (2005), Crystallization and very rapid exhumation of the youngest Alpine eclogites (Tauern Window, Eastern Alps) from Rb/Sr mineral assemblage analysis, *Contrib. Mineral. Petrol.*, **149**, 699–712, doi:10.1007/s00410-005-0676-5.
- Glodny, J., A. Kühn, and H. Austrheim (2008a), Diffusion versus recrystallization processes in Rb-Sr geochronology: Isotopic relics in eclogite facies rocks, Western Gneiss region, Norway, *Geochim. Cosmochim. Acta*, **72**, 506–525, doi:10.1016/j.gca.2007.10.021.
- Glodny, J., A. Kühn, and H. Austrheim (2008b), Geochronology of fluid-induced eclogite and amphibolite facies metamorphic reactions in a subduction-collision system, Bergen Arcs, Norway, *Contrib. Mineral. Petrol.*, **156**, 27–48, doi:10.1007/s00410-007-0272-y.
- Glodny, J., U. Ring, and A. Kühn (2008c), Coeval high-pressure metamorphism, thrusting, strike-slip, and extensional shearing in the Tauern Window, Eastern Alps, *Tectonics*, **27**, TC4004, doi:10.1029/2007TC002193.
- Goffé, B., and R. Bousquet (1997), Ferrocapholite, chloritoïde et lawsonite dans les métapelites des unités du Versoyen et du Petit St. Bernard (zone Valaisanne, Alpes occidentales), *Schweiz. Mineral. Petrogr. Mitt.*, **77**, 137–147.
- Goffé, B., and R. Oberhänsli (1992), Ferro- and magnesio-capholite in the “Bündnerschiefer” of the eastern central Alps (Grisons and Engadine Window), *Eur. J. Mineral.*, **4**, 835–838.
- Goffé, B., R. Bousquet, P. Henry, and X. Le Pichon (2003), Effect of the chemical composition of the crust on the metamorphic evolution of orogenic wedges, *J. Metamorph. Geol.*, **21**, 123–141, doi:10.1046/j.1525-1314.2003.00422.x.
- Gouzu, C., T. Itaya, H. Hyodo, and T. Matsuda (2006), Excess  $^{40}\text{Ar}$ -free phengite in ultrahigh-pressure metamorphic rocks from the Lago di Cignana area, Western Alps, *Lithos*, **92**, 418–430, doi:10.1016/j.lithos.2006.03.056.
- Hermann, J., A. Rubatto, and V. Trommsdorff (2006), Sub-solidus Oligocene zircon formation in garnet peridotite during fast decompression and fluid infiltration (Duria, central Alps), *Mineral. Petrol.*, **88**, 181–206, doi:10.1007/s00710-006-0155-3.
- Herwartz, D., C. Münker, E. E. Scherer, T. J. Nagel, J. Pleuger, and N. Froitzheim (2008), Lu-Hf garnet geochronology of eclogites from the Balma Unit (Pennine Alps): Implications for Alpine paleotectonic reconstructions, *Swiss J. Geosci.*, **101**, Suppl., S173–S189.
- Hess, J. C., and H. J. Lippolt (1994), Compilation of K-Ar measurements on HD-B1 standard biotite, 1994 status report, in *Phanerozoic Time Scale, Bull. Liais. Inf.* **122**, IUGS Subcomm. Geochronol., Paris.
- Hitz, L., and O. A. Pfiffner (1997), Geologic interpretation of the seismic profiles of the Eastern Traverse (lines E1–E3, E7–E9), eastern Swiss Alps, in *Deep Structure of the Swiss Alps—Results of NRP 20*, edited by O. A. Pfiffner et al., pp. 73–100, Birkhäuser, Basel.
- Hodges, K. V., W. E. Hames, and S. A. Bowring (1994),  $^{40}\text{Ar}/^{39}\text{Ar}$  age gradients in micas from a high-temperature low-pressure metamorphic terrain—evidence for very slow cooling and implications for the interpretation of age spectra, *Geology*, **22**, 55–58, doi:10.1130/0091-7613(1994)022<0055:AAAGIM>2.3.CO;2.
- Hunziker, J. C., M. Frey, N. Clauer, R. D. Dallmeyer, H. Friedrichsen, W. Flehmig, K. Hochstrasser, P. Roggwiler, and H. Schwander (1986), The evolution of illite to muscovite: Mineralogical and isotopic data from the Glarus Alps, Switzerland, *Contrib. Mineral. Petrol.*, **92**, 157–180, doi:10.1007/BF00375291.
- Hunziker, J. C., J. Desmons, and A. J. Hurford (1992), Thirty-two years of geochronological work in the central and Western Alps: A review on seven maps, *Mem. Geol. Lausanne*, **13**, 1–59.
- Hurford, A. J. (1986), Cooling and uplift patterns in the Lepontine Alps, south-central Switzerland and an age of vertical movement on the Insubric fault line, *Contrib. Mineral. Petrol.*, **92**, 413–427, doi:10.1007/BF00374424.
- Hurford, A. J. (1990), Standardization of fission track dating calibration: Recommendation by the Fission Track Working Group of the IUGS Subcommittee on Geochronology, *Chem. Geol.*, **80**, 171–178.
- Ishizuka, O. (1998), Vertical and horizontal variations of the fast neutron flux in a single irradiation capsule and their significance in the laser-heating  $^{40}\text{Ar}/^{39}\text{Ar}$  analysis: Case study for the hydraulic rabbit facility of the JMTR reactor, Japan, *Geochem. J.*, **32**, 243–252.
- Ishizuka, O., M. Yuasa, and K. Uto (2002), Evidence of porphyry copper-type hydrothermal activity from a submerged remnant back-arc volcano of the Izu-Bonin arc—Implications for the volcanotectonic history of back-arc seamounts, *Earth Planet. Sci. Lett.*, **198**, 381–399, doi:10.1016/S0012-821X(02)00515-0.
- Jäger, E., E. Niggli, and E. Wenk (1967), Rb-Sr Altersbestimmungen an Glimmern der Zentralalpen, *Beitr. Geol. Kt. Schweiz.*, **134**, 67 pp., Kümmerly und Frey, Bern.
- Jamieson, R. A., C. Beaumont, P. Fullsack, and B. Lee (1998), Barrovian regional metamorphism: Where's the heat?, in *What Drives Metamorphism and Metamorphic Reactions?*, edited by P. J. Treloar and P. J. O'Brian, *Geol. Soc. Special Publ.*, **138**, 23–51.
- Janots, E., F. Negro, F. Brunet, B. Goffé, M. Engi, and M. L. Bouybaouene (2006), Evolution of the REE mineralogy in HP-LT metapelites of the Sebte complex, Rif, Morocco: Monazite stability and geochronology, *Lithos*, **87**, 214–234, doi:10.1016/j.lithos.2005.06.008.
- Janots, E., M. Engi, D. Rubatto, A. Berger, C. Gregory, and M. K. Rahn (2009), Metamorphic rates in collisional orogeny from in situ allanite and monazite dating, *Geology*, **37**, 11–14, doi:10.1130/G25192A.1.
- Jeong, G. Y., C. S. Cheong, and J. Kim (2006), Rb-Sr and K-Ar systems of biotite in surface environments regulated by weathering processes with implications for isotopic dating and hydrological cycles of Sr isotopes, *Geochim. Cosmochim. Acta*, **70**, 4734–4749, doi:10.1016/j.gca.2006.07.012.
- Jolivet, L., B. Goffé, R. Bousquet, R. Oberhänsli, and A. Michard (1998), Detachments in high-pressure mountain belts, Tethyan examples, *Earth Planet. Sci. Lett.*, **160**, 31–47, doi:10.1016/S0012-821X(98)00079-X.
- Kelley, S. P., N. O. Arnaud, and S. P. Turner (1994), High spatial resolution  $^{40}\text{Ar}/^{39}\text{Ar}$  investigations using an ultra-violet laser probe extraction technique, *Geochim. Cosmochim. Acta*, **58**, 3519–3525, doi:10.1016/0016-7037(94)90103-1.
- Kurz, W., R. Handler, and C. Bertoldi (2008), Tracing the exhumation of the Eclogite Zone (Tauern Window, Eastern Alps) by  $^{40}\text{Ar}/^{39}\text{Ar}$  dating of white mica in eclogites, *Swiss J. Geosci.*, **101**, Suppl., S191–S206.
- Lanphere, M. A., and H. Baadsgaard (2001), Precise K-Ar,  $^{40}\text{Ar}/^{39}\text{Ar}$ , Rb-Sr and U/Pb mineral ages from the 27.5 Ma Fish Canyon Tuff reference standard, *Chem. Geol.*, **175**, 653–671, doi:10.1016/S0009-2541(00)00291-6.
- Lanphere, M. A., and G. B. Dalrymple (1976), Identification of excess  $^{40}\text{Ar}$  by  $^{40}\text{Ar}/^{39}\text{Ar}$  age spectrum technique, *Earth Planet. Sci. Lett.*, **32**, 141–148, doi:10.1016/0012-821X(76)90052-2.
- Le Pichon, X., F. Bergerat, and M.-J. Roulet (1988), Plate kinematics and tectonics leading to the Alpine belt formation: A new analysis, in *Processes in Continental Lithospheric Deformation*, edited by S. P. Clark et al., *Spec. Pap. Geol. Soc. Am.*, **218**, 111–131.
- Liati, A., and N. Froitzheim (2006), Assessing the Valais Ocean, Western Alps: U-Pb SHRIMP zircon geochronology of eclogite in the Balma unit, on top of the Monte Rosa nappe, *Eur. J. Mineral.*, **18**, 299–308, doi:10.1127/0935-1221/2006/0018-0299.
- Liati, A., N. Froitzheim, and C. M. Fanning (2005), Jurassic ophiolites within the Valais domain of the Western and central Alps: Geochronological evidence for re-rifting of oceanic crust, *Contrib. Mineral. Petrol.*, **149**, 446–461, doi:10.1007/s00410-005-0658-7.
- Lihou, J. C., and P. A. Allen (1996), Importance of inherited rift margin structures in the early North Alpine Foreland Basin, Switzerland, *Basin Res.*, **8**, 425–442, doi:10.1046/j.1365-2117.1996.00244.x.
- Livi, K. J. T., J. M. Ferry, D. R. Veblen, M. Frey, and J. A. D. Connolly (2002), Reactions and physical conditions during metamorphism of Liassic aluminous black shales and marls in central Switzerland, *Eur. J. Mineral.*, **14**, 647–672, doi:10.1127/0935-1221/2002/0014-0647.
- Maluski, H., and P. Monié (1988),  $^{40}\text{Ar}/^{39}\text{Ar}$  laser-probe multidating inside single biotites of a Variscan orthogneiss (Pinet Massif Central, France), *Chem. Geol.*, **73**, 245–263.
- McDougall, I., and T. M. Harrison (1999), *Geochronology and Thermochronology by the  $^{40}\text{Ar}/^{39}\text{Ar}$  Method*, 269 pp., Oxford Univ. Press, New York.
- Michalski, I., and M. Soom (1990), The Alpine thermotectonic evolution of the Aar and Gotthard massifs, central Switzerland: Fission track ages on zircon and apatite and K-Ar mica ages, *Schweiz. Mineral. Petrogr. Mitt.*, **70**, 373–387.
- Milnes, A. G. (1974), Structure of the Pennine zone (central Alps)—A new working hypothesis, *Geol. Soc. Am. Bull.*, **85**, 1727–1732, doi:10.1130/0016-7606(1974)85<1727:SOTPZC>2.0.CO;2.
- Müller, W., R. D. Dallmeyer, F. Neubauer, and M. Thöni (1999), Deformation-induced resetting of Rb/Sr and  $^{40}\text{Ar}/^{39}\text{Ar}$  mineral systems in a low-grade, polymetamorphic terrane (Eastern Alps, Austria), *J. Geol. Soc.*, **156**, 261–278, doi:10.1144/gsjgs.156.2.0261.
- Nabholz, W. K. (1945), Geologie der Bündnerschiefergebirge zwischen Rheinwald, Valsler- und Saftental, *Eclogae Geol. Helv.*, **38**, 1–119.
- Nagel, T. J. (2008), Tertiary subduction, collision and exhumation recorded in the Adula nappe, central Alps, in *Tectonic Aspects of the Alpine-Dinaride-Carpathian System*, edited by S. Siegesmund et al., *Geol. Soc. Spec. Publ.*, **298**, 365–392.
- Nänny, P. (1948), Zur Geologie der Prättigauschiefer zwischen Rhätikon und Plessur, Ph.D. thesis, Univ. Zürich, Zurich, Switzerland.
- Niggli, E. (1970), Alpine Metamorphose und alpine Gebirgsbildung, *Fortschr. Mineral.*, **47**, 16–26.

- Oberhänsli, R. (1978), Chemische Untersuchungen an Glaukophan-führenden basischen Gesteinen aus den Bündnerschiefern Graubündens, *Schweiz. Mineral. Petrogr. Mitt.*, 58, 139–156.
- Oberhänsli, R. (1994), Subducted and obducted ophiolites of the central Alps: Paleotectonic implications deduced by their distribution and metamorphic overprint, *Lithos*, 33, 109–118, doi:10.1016/0024-4937(94)90056-6.
- Oberhänsli, R., B. Goffé, and R. Bousquet (1995), Record of a HP-LT metamorphic evolution in the Valais zone: Geodynamic implications, in *Studies on Metamorphic Rocks and Minerals of the Western Alps. A Volume in Memory of Ugo Pognante*, *Boll. Mus. Reg. Sci. Nat. Torino*, vol. 13, edited by B. Lombardo, pp. 221–239, Mus. Reg. di Sci. Nat., Turin, Italy.
- Oberhänsli, R., et al. (2004), Metamorphic structure of the Alps, 1:1,000,000, Explanatory note to the map “Metamorphic structure of the Alps,” *Mitt. Oesterr. Geol. Ges.*, vol. 149, edited by R. Oberhänsli, Comm. for the Geol. Map of the World, Paris.
- Parra, T., O. Vidal, and P. Agard (2002), A thermodynamic model for Fe-Mg dioctahedral K white micas using data from phase-equilibrium experiments and natural pelitic assemblages, *Contrib. Mineral. Petrol.*, 143, 706–732.
- Philippot, P., J. Blichert-Toft, A. Perchuk, S. Costa, and V. Gerasimov (2001), Lu-Hf and Ar-Ar chronometry supports extreme rate of subduction zone metamorphism deduced from geospeedometry, *Tectonophysics*, 342, 23–38, doi:10.1016/S0040-1951(01)00155-X.
- Probst, P. (1980), Die Bündnerschiefer des nördlichen Penninikums zwischen Valser Tal und Passo di San Giacomo, *Beitr. Geol. Kt. Schweiz*, 153, 64 pp., Kümmerly und Frey, Bern.
- Purdy, J. W., and E. Jäger (1976), K-Ar ages on rock-forming minerals from the Central Alps, *Mem. Ist. Geol. Mineral. Univ. Padova*, 30, 1–32.
- Ratschbacher, L., C. Dingeldeya, C. Miller, B. R. Hacker, and M. O. McWilliams (2004), Formation, subduction, and exhumation of Penninic oceanic crust in the Eastern Alps: Time constraints from  $^{40}\text{Ar}/^{39}\text{Ar}$  geochronology, *Tectonophysics*, 394, 155–170, doi:10.1016/j.tecto.2004.08.003.
- Roselle, G. T., M. Thüring, and M. Engi (2002), MELONPIT: A finite element code for simulating tectonic mass movement and heat flow within subduction zones, *Am. J. Sci.*, 302, 381–409, doi:10.2475/ajs.302.5.381.
- Scaillet, S. (1996), Excess  $^{40}\text{Ar}$  transport scale and mechanism in high-pressure phengites: A case study from an eclogitized metabasite of the Dora Maira nappe, Western Alps, *Geochim. Cosmochim. Acta*, 60, 1075–1090, doi:10.1016/0016-7037(95)00440-8.
- Schmid, S. M., P. Rück, and G. Schreurs (1990), The significance of the Schams nappes for the reconstruction of the paleotectonic and orogenic evolution of the Penninic zone along the NFP-20 East traverse (Grisons, eastern Switzerland), in *Deep Structure of the Alps*, edited by F. Roure et al., *Mem. Soc. Fr.*, 156, 263–287.
- Schmid, S. M., O. A. Pfiffner, N. Froitzheim, G. Schönborn, and E. Kissling (1996), Geophysical-geological transect and tectonic evolution of the Swiss-Italian Alps, *Tectonics*, 15, 1036–1064, doi:10.1029/96TC00433.
- Schmid, S. M., B. Fügenschuh, E. Kissling, and R. Schuster (2004), Tectonic map and overall architecture of the Alpine orogen, *Eclogae Geol. Helv.*, 97, 93–117, doi:10.1007/s00015-004-1113-x.
- Schmitz, S., A. Möller, M. Wilke, W. Malzer, B. Kanngiesser, R. Bousquet, A. Berger, and S. Schefer (2009), 3D synchrotron radiation x-ray fluorescence (SRXRF) chemical U-Th-Pb dating of monazite, *Eur. J. Mineral.*, 5, 927–946.
- Schreurs, G. (1993), Structural analysis of the Schams nappes and adjacent tectonic units: Implications for the orogenic evolution of the Pennine zone in eastern Switzerland, *Bull. Soc. Geol. Fr.*, 164, 415–435.
- Sherlock, S., and S. Kelley (2002), Excess argon evolution in HP-LT rocks: A UVLAMP study of phengite and K-free minerals, NW Turkey, *Chem. Geol.*, 182, 619–636, doi:10.1016/S0009-2541(01)00345-X.
- Stampfli, G. M. (1993), Le Briançonnais: Terrain exotique dans les Alpes?, *Eclogae Geol. Helv.*, 86, 1–45.
- Stampfli, G. M., J. Mosar, D. Marquer, R. Marchant, T. Baudin, and G. Borel (1998), Subduction and obduction processes in the Swiss Alps, *Tectonophysics*, 296, 159–204, doi:10.1016/S0040-1951(98)00142-5.
- Steck, A., and J. C. Hunziker (1994), The tertiary structural and thermal evolution of the Central Alps—compressional and extensional structures in an orogenic belt, *Tectonophysics*, 238, 229–254, doi:10.1016/0040-1951(94)90058-2.
- Steinmann, M. C. (1994), Die nordpenninischen Bündnerschiefer der Zentralalpen Graubündens: Tektonik, Stratigraphie und Beckenentwicklung, Ph.D. thesis, ETH Zürich, Zurich, Switzerland.
- Steinmann, M., and P. Stille (1999), Geochemical evidence for the nature of the crust beneath the eastern North Penninic basin of the Mesozoic Tethys Ocean, *Geol. Rundsch.*, 87, 633–643, doi:10.1007/s005310050236.
- Sudo, M., K. Uto, K. Anno, O. Ishizuka, and S. Uchiumi (1998), SOR193 biotite: A new mineral standard for K-Ar dating, *Geochem. J.*, 32, 49–58.
- Tagami, T., and C. Shimada (1996), Natural long-term annealing of the fission-track system around a granitic pluton, *J. Geophys. Res.*, 101, 8245–8255, doi:10.1029/95JB02885.
- Thöni, M. (2006), Dating eclogite-facies metamorphism in the Eastern Alps—Approaches, results, interpretations: A review, *Mineral. Petrol.*, 88, 123–148, doi:10.1007/s00710-006-0153-5.
- Todd, C. S., and M. Engi (1997), Metamorphic field gradients in the central Alps, *J. Metamorph. Geol.*, 15, 513–530, doi:10.1111/j.1525-1314.1997.00038.x.
- Tricart, P. (1984), From passive margin to continental collision: A tectonic scenario for the Western Alps, *Am. J. Sci.*, 284, 97–120.
- Trümpy, R. (1960), Paleotectonic evolution of the central and Western Alps, *Geol. Soc. Am. Bull.*, 71, 843–908, doi:10.1130/0016-7606(1960)71[843:PEOTCA]2.0.CO;2.
- Uto, K., O. Ishizuka, A. Matsumoto, H. Kamioka, and S. Togashi (1997), Laser-heating  $^{40}\text{Ar}/^{39}\text{Ar}$  dating system of the Geological Survey of Japan: System outline and preliminary results, *Bull. Geol. Surv. Jpn.*, 48, 23–46.
- Vernon, A. J., P. A. van der Beek, H. D. Sinclair, and M. K. Rahn (2008), Increase in late Neogene denudation of the European Alps confirmed by analysis of a fission-track thermochronology database, *Earth Planet. Sci. Lett.*, 270, 316–329, doi:10.1016/j.epsl.2008.03.053.
- Vidal, O., and T. Parra (2000), Exhumation paths of high-pressure metapelites obtained from local equilibria for chlorite-phengite assemblages, *Geol. J.*, 35, 139–161, doi:10.1002/gj.856.
- Villa, I. M. (1998), Isotopic closure, *Terra Nova*, 10, 42–47, doi:10.1046/j.1365-3121.1998.00156.x.
- Villa, I. M. (2006), From nanometer to megameter: Isotopes, atomic scale processes, and continent-scale tectonic models, *Lithos*, 87, 155–173, doi:10.1016/j.lithos.2005.06.012.
- von Blanckenburg, F. (1992), Combined high-precision chronometry and geochemical tracing using accessory minerals: Applied to the central-Alpine Bergell intrusion (central Europe), *Chem. Geol.*, 100, 19–40, doi:10.1016/0009-2541(92)90100-J.
- Wenk, E. (1970), Zur Regionalmetamorphose und Ultrametamorphose im Lepontin, *Fortschr. Mineral.*, 47, 34–51.
- Wiederkehr, M., R. Bousquet, S. M. Schmid, and A. Berger (2008), From subduction to collision: Thermal overprint of HP/LT meta-sediments in the north-eastern Lepontine Dome (Swiss Alps) and consequences regarding the tectono-metamorphic evolution of the Alpine orogenic wedge, *Swiss J. Geosci.*, 101, Suppl., S127–S155.
- Wiederkehr, M. (2009), From subduction to collision: a combined metamorphic, structural and geochronological study of polymetamorphic metasediments at the NE edge of the Lepontine dome (Swiss central Alps), Ph.D. thesis, Univ. Basel, Basel.
- Wijbrans, J. R., and I. McDougall (1986),  $^{40}\text{Ar}/^{39}\text{Ar}$  dating of white micas from an Alpine high-pressure metamorphic belt on Naxos (Greece)—The resetting of the argon isotopic system, *Contrib. Mineral. Petrol.*, 93, 187–194, doi:10.1007/BF00371320.
- Ziegler, W. (1956), Geologische Studien in den Fylschgebieten des Oberhalbsteins (Graubünden), *Eclogae Geol. Helv.*, 49, 1–78.

A. Berger, Institut for Geografi og Geologi, Københavns Universitet, Øster Voldgade 10, DK-1350 København K, Denmark.

R. Bousquet and M. Sudo, Institut für Geowissenschaften, Universität Potsdam, Karl-Liebknecht-Strasse 24/25, D-14476 Potsdam, Germany.  
S. M. Schmid, Institut für Geologische Wissenschaften, Freie Universität Berlin, Malteserstrasse 74-100, D-12249 Berlin, Germany.

M. Wiederkehr, Geologisch-Paläontologisches Institut, Universität Basel, Bernoullistrasse 32, CH-4056 Basel, Switzerland. (m.wiederkehr@unibas.ch)